

# ABSTRACT

## **KONG, JIAN. Infrared-Based Temperature Measurement in Ceramics Grinding and Diesel Exhaust Aftertreatment Filters. (Under the direction of Albert J. Shih)**

Non-contact remote-sensing radiation thermometry was used in the applications of temperature measurement in ceramics grinding and diesel exhaust aftertreatment filters.

Results of temperature measurements by analysis of the thermal emission spectra generated during grinding and subsequently transmitted through partially stabilized zirconia workpiece are presented. Portions of emitted visible and near-infrared spectra were collected with spectrometers. Source temperatures were determined by fitting the scaled spectrometer output spectra to blackbody curves. Simulations showed that the effective temperatures determined by this method will be strongly biased toward hot-spot (flash) temperatures, which are expected to occur at the grinding grit-workpiece interface. Hot-spot temperatures on the order of 3000 K were obtained for grinding with both SiC and diamond wheels. These high temperatures modify the grinding process and the phase content of grinding chips.

The in-situ measurement of the temperature distribution on the cavity wall surface in diesel exhaust aftertreatment filters using the infrared radiation thermometry was developed. The temperature measurement system consists of a sapphire fiber with 45° angled tip, PbS/PbSe two-color sensor, and data conditioning and acquisition device. A calibration technique using the blackbody cavity was developed. Calibration curves were generated between 80 to 400°C, the temperature range of special interest for applications in catalyzed diesel exhaust aftertreatment filters. One-color and two-color radiation thermometry methods were both employed to compare and validate temperature measurement results. The

wall surface temperature of a microwave-heated ceramic filter was measured at four locations. This study demonstrates the feasibility of using the infrared thermometry for non-contact temperature measurement at a specific region within the cavity of diesel exhaust aftertreatment filters.

Based on the above temperature measurement results, the infrared thermometry method was applied to study the temperature distribution in microwave heating of diesel particulate filters. Temperature measurement tests were conducted in integrated multi-channel fiber optic infrared temperature measurement and microwave heating systems. The silica light-pipes, which are transparent to electromagnetic field, were used to collect the infrared radiation from different locations inside filter cavity. One-color thermometry method was implemented to convert the measured radiation into temperatures. The temporal and spatial distributions of three diesel particulate filters heated by microwave were studied. Experimental results show the non-uniform heating across the filter. The interaction between catalyst, soot loading, and microwave power varies the heating pattern and temperature distribution. During a 600 s heating period, a 1 kW microwave power setting is able to raise the temperatures above 200°C in most area of a catalyzed filter with soot loading.

**Infrared-Based Temperature Measurement in Ceramics  
Grinding and Diesel Exhaust Aftertreatment Filters**

by  
**Jian Kong**

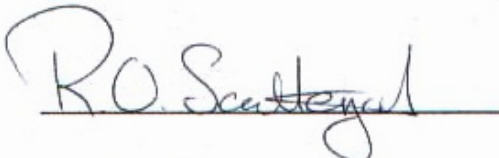
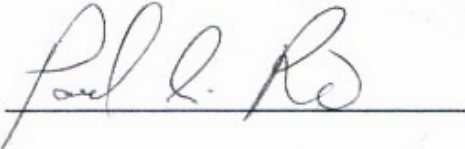
A dissertation submitted to the Graduate Faculty of  
North Carolina State University  
in partial fulfillment of the  
requirements for the Degree of  
Doctor of Philosophy

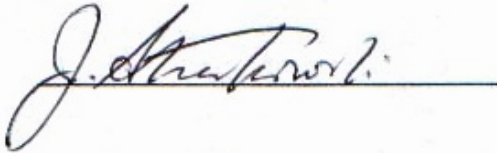
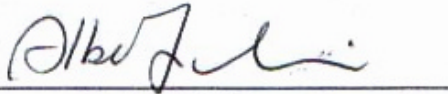
**Department of Mechanical and Aerospace Engineering**

Raleigh, NC

2003

Approved by:

  
\_\_\_\_\_  
  
\_\_\_\_\_

  
\_\_\_\_\_  
  
\_\_\_\_\_  
Chair of Advisory Committee

## **Biography**

Jian Kong was born in Tieling, a small town in Northeast China. He is the only child in the Kong family.

Jian received a Bachelor of Science in Mechanical Engineering from Tongji University in July 1997 in Shanghai, China, and a Master of Science in Mechanical Engineering from Tongji University in March 2000. During his college years, he showed great talent in his study and interest in scientific research. He won two cups for the University in undergraduate and graduate research competitions in 1997 and 1998, respectively. In 2000, he came to U.S. and continued his study at The University of Kansas. In 2001, Dr. Albert J. Shih recruited him as a Ph.D. student in Mechanical Engineering Department at North Carolina State University. Jian has spent the last three years in pursuing his doctoral degree. He will graduate at the end of 2003.

## Acknowledgments

I would like to thank Dr. Albert J. Shih for giving me the opportunity to explore this topic, providing guidance and suggestions throughout this research project, and helping me develop the ideas that made the research a success.

Thanks to my committee members, Dr. John Strenkowski, Dr. Paul Ro, and Dr. Ron Scattergood. I appreciate the contribution of your time and efforts.

Thanks to Adam Curry for his previous research work that helped shape the direction of this project.

Thanks to Brian J. Boothe for his technical assistance in fiber optic sensor calibration experiments.

I would also like to thank my parents for their unfailing support and encouragement.

Portion of this research was sponsored by the User program of the High Temperature Material Lab, Oak Ridge National Lab and, the Heavy Vehicle Propulsion Systems Materials Program, Office of Transportation Technologies, US Department of Energy.

The assistance provided by Richard D. Nixdorf of Industrial Ceramic Solutions, LLC, for providing the ceramic filter sample, is gratefully acknowledged.

Thanks to Dr. Matthew Henrichsen, Randy J. Stafford at Cummins Technical Enter for their technical support. The management support from Thomas M. Yonushonis at Cummins Technical Center and Dr. D. Raymond Johnson at Oak Ridge National Lab is particularly acknowledged.

## TALBE OF CONTENTS

<b>LIST OF TABLES.....</b>	<b>VI</b>
<b>LIST OF FIGURES .....</b>	<b>VII</b>
<b>CHAPTER 1. INTRODUCTION.....</b>	<b>1</b>
1.1. BACKGROUND OF RADIATION THERMOMETRY .....	1
1.2. OVERVIEW .....	5
REFERENCES .....	7
<b>CHAPTER 2. GRINDING TEMPERATURE MEASUREMENTS IN MGO-PSZ USING INFRARED SPECTROMETRY.....</b>	<b>12</b>
2.1. INTRODUCTION .....	12
2.2. THERMAL EFFECTS IN GRINDING .....	14
2.3. EXPERIMENTAL PROCEDURE.....	18
2.4. ANALYSIS METHOD AND RESULTS .....	22
2.5. DISCUSSION .....	30
2.6. SUMMARY AND CONCLUSIONS.....	38
REFERENCES .....	39
<b>CHAPTER 3. INFRARED THERMOMETRY FOR DIESEL EXHAUST AFTERTREATMENT FILTER TEMPERATURE MEASUREMENT .....</b>	<b>41</b>
3.1. INTRODUCTION .....	41
3.2. INFRARED-BASED TEMPERATURE MEASUREMENT SYSTEM .....	44
3.2.1 <i>Single Crystal Sapphire Fiber</i> .....	44
3.2.2 <i>PbS/PbSe Two-Color Infrared Sensor</i> .....	47
3.3. TEMPERATURE MEASUREMENT AND SYSTEM CALIBRATION .....	49
3.3.1 <i>Radiation Thermometry Methods</i> .....	49
3.3.2 <i>Temperature Measurement Strategy</i> .....	51
3.4. CALIBRATION.....	52
3.5. FILTER HEATING AND TEMPERATURE MEASUREMENT EXPERIMENT SETUP .....	54
3.6. TEMPERATURE MEASUREMENT RESULTS AND DISCUSSION.....	58
3.7. LOW TEMPERATURE MEASUREMENT CAPABILITY IMPROVEMENT .....	62
3.8. PARASITIC HEATING EFFECT .....	64
3.9. CONCLUDING REMARKS .....	66
REFERENCES .....	67
<b>CHAPTER 4. INFRARED THERMOMETRY MEASUREMENT OF TEMPERATURE DISTRIBUTION IN MICROWAVE REGENERATION OF DIESEL PARTICULATE FILTERS.....</b>	<b>69</b>
4.1. INTRODUCTION .....	69

4.2. SYSTEM COMPONENT DESCRIPTION.....	71
4.2.1. <i>Multi Channel Infrared Fiber Optic Temperature Measurement System</i> .....	71
4.2.2. <i>Microwave Heating System</i> .....	73
4.3. TEMPERATURE MEASUREMENT CALIBRATION AND VALIDATION.....	75
4.3.1. <i>One-Color Temperature Measurement Calibration</i> .....	75
4.3.2. <i>Filter Material Opacity Test</i> .....	75
4.3.3. <i>Filter Heating Repeatability Tests</i> .....	76
4.4. FILTER HEATING AND TEMPERATURE MEASUREMENT EXPERIMENTAL SETUP.....	79
4.5. TEMPERATURE MEASUREMENT RESULTS AND DISCUSSION.....	80
4.5.1. <i>Filter F1 -- Uncatalyzed Filter with Soot Loading</i> .....	81
4.5.2. <i>Filter F2 -- Catalyzed Filter without Soot Loading</i> .....	84
4.5.3. <i>Filter F3 -- Catalyzed Filter with Soot Loading</i> .....	86
4.6. CONCLUDING REMARKS .....	88
REFERENCES .....	88
<b>CHAPTER 5. CONCLUSIONS.....</b>	<b>91</b>
APPENDIX .....	94

## LIST OF TABLES

<i>Table 2.1. Summary of the results for the temperature measurements. Grinding conditions given: Wheel rpm (Speed), downfeed (Feed), material removal rate per mm of wheel width (MRR). The grinding table speed was 150 mm/s for all tests. ....</i>	<i>29</i>
--	-----------



## LIST OF FIGURES

<i>Figure 2.1. Phase diagram for MgO-PSZ [19].</i>	16
<i>Figure 2.2. (a) Schematic of the grinding test setup and (b) Photograph of the setup.</i>	19
<i>Figure 2.3. Blackbody radiation curves for the temperatures indicated. Scaling (vertical shift) of the <math>R(\lambda)</math> spectral data produces a best fit for 2000 K, as indicated.</i>	23
<i>Figure 2.4. Top frame shows the measured spectrometer output, <math>R(\lambda)</math> vs. <math>\lambda</math>, and the best-fit blackbody curve (solid line). Bottom frame shows the least-squares fit (solid-line) and effective temperature obtained using Eq. (2.5). Wheel speed, downfeed and sample thickness are indicated for each test. (a)-(c) SiC grinding wheel and (d) Diamond grinding wheel.</i>	26
<i>Figure 2.5. Simulation results for determination of the effective temperature. (a) Area fraction of hot spots was varied as indicated and (b) Background hot spot emissivity ratio was varied as indicated.</i>	32
<i>Figure 2.6. Best-fit blackbody curves for a range of temperatures. The <math>R(\lambda)</math> vs. <math>\lambda</math> spectrometer data used is the same as that shown in Fig. 2.4(c).</i>	34
<i>Figure 2.7. SEM micrographs of grinding chips obtained using a SiC grinding wheel. The grinding conditions were: 0.0127 mm downfeed and 2.91 mm<sup>2</sup>/s material removal rate for both (a) and (b).</i>	37
<i>Figure 3.1. The application of PbS-PbSe two-color sensor and sapphire optical fiber for measurement of diesel exhaust aftertreatment filter temperature; (a) experiment setup (b) close-up view of the two-color sensor, chopper, and sapphire fiber.</i>	42
<i>Figure 3.2. Sapphire fiber with 45° angled tip.</i>	45
<i>Figure 3.3. Goniometric characteristics of 45° angled tip sapphire optical fiber [3].</i>	46
<i>Figure 3.4. The relative intensity of the detectors vs. wavelength.</i>	48
<i>Figure 3.5. PbS and PbSe detector voltage output vs. temperature.</i>	49
<i>Figure 3.6. Oxidized Inconel cavity as the blackbody for infrared sensor calibration.</i>	53
<i>Figure 3.7. Blackbody calibration results; (a) one-color calibration data points and curves and, (b) two-color calibration data points and curves.</i>	55

<i>Figure 3.8. Setup for microwave heating temperature measurement; (a) overview of the sensor, optical fiber, microwave heater, and data acquisition and (b) entry and positioning holes for optical fiber.</i>	56
<i>Figure 3.9. Setup for filter and optical fiber inside the microwave heater; (a) front view of the filter and the designation of cavity I and II and (b) side view of filter with the center, C, and side, S, locations of fiber tip.</i>	57
<i>Figure 3.10. Temperature repeatability at location IIS.</i>	59
<i>Figure 3.11. Temperature vs. time at four locations during microwave heating tests.</i>	61
<i>Figure 3.12. The application of lock-in amplifier for improvement of low temperature measurement capability.</i>	62
<i>Figure 3.13. Blackbody calibration result of PbS channel with a lock-in amplifier.</i>	63
<i>Figure 3.14. Temperature vs. time results of one-color method w/o lock-in amplifier and two color method.</i>	64
<i>Figure 3.15. Experiment setup to test the scattered light around the fiber.</i>	65
<i>Figure 4.1. Experimental setup of multi channel infrared fiber optic sensor for the measurement of diesel exhaust aftertreatment filter temperature; (a) cross-sectional view and (b) top view of the optical fiber insertion locations.</i>	72
<i>Figure 4.2. Silica light-pipe with bent and polished tip.</i>	73
<i>Figure 4.3. Overview of the developed bench scale microwave heating system.</i>	74
<i>Figure 4.4. Results of temperature heating repeatability tests; (a) repeatable temperature curves at 500 W microwave power setting and, (b) unrepeatable temperature curves at 1 kW microwave power setting.</i>	78
<i>Figure 4.5. Setup for microwave heating temperature measurement; (a) Thermometers and transmission fibers (b) close-up view of the silica light-pipes insertion.</i>	79
<i>Figure 4.6. Temperature vs. time results at 36 locations in filter F1 during microwave heating tests.</i>	83
<i>Figure 4.7. Temperature vs. time results at 36 locations in filter F2 during microwave heating tests.</i>	85
<i>Figure 4.8. Temperature vs. time results at 36 locations in filter F3 during microwave heating tests.</i>	87
<i>Figure A1. Simulation results for deviation vs. temperature.</i>	96

## CHAPTER 1. INTRODUCTION

### 1.1. Background of Radiation Thermometry

Radiation thermometry is the measurement of an object temperature by quantification of the electromagnetic radiation emitted from the object. It is used to measure the object temperature without any physical contact. Radiation thermometry is a widely used temperature measurement method and has been applied in a wide variety of applications [1-3]. Radiation thermometry exhibits response time shorter than contact sensors and is usually employed to measure the temperature of objects that are difficult to reach by contact detection due to hostile environments, geometry limitations, and/or safety hazards. Radiation thermometry can also measure the temperature of moving samples or objects kept in a vacuum.

Radiation thermometers measure absolute intensity of the radiation emanating from a target surface. A calibration method is necessary to convert the measured radiation output signal, generally in DC voltage, to temperature. The relationship between the radiance and temperature of a blackbody is described by the Planck's law.

$$L_{\lambda,b}(\lambda,T) = \frac{c_{1L}}{\lambda^5 (e^{\frac{c_2}{\lambda T}} - 1)} \quad (1.1)$$

where  $c_{1L} = 1.191 \times 10^8 \text{ W} \cdot \mu\text{m}^4 \cdot \text{m}^{-2} \cdot \text{sr}^{-1}$  and  $c_2 = 1.439 \times 10^4 \text{ } \mu\text{m} \cdot \text{K}$  are the first and second radiation constants and  $T$  is the absolute temperature. Planck's law of blackbody radiation is the foundation of radiation thermometry [4-5].

In its most basic form, a thermometer is a spectrometer which records a voltage  $V(\lambda)$  in response to radiation emitting from a blackbody. In practice, the target seldom approximates a blackbody radiator and the target environment, comprised of its surroundings and the atmosphere in its line of sight, is not as well controlled as during the calibration process. The radiant flux exiting from the target surface is due to three processes: emission from the non-black target having a spectral emissivity less than unity, reflection of irradiation originating from the hotter surroundings and from a participating atmosphere, and absorption or emission by atmospheric gases in the sight path. For this situation, the radiation thermometer output will be a signal which, through the calibration algorithm, corresponds to the temperature of an equivalent blackbody. It is evident that the user needs information on the surroundings and the environment in order to relate the indicated temperature to the true temperature of the target surface. One of the most important parameters that strongly affects the measurement accuracy of radiation thermometers is the target emissivity, which often varies with spectral wavelength, temperature, surface property and, in some cases, time [3-5].

For a variety of different scientific and industrial applications, radiation thermometry can be divided into several categories. According to the number of sampled spectral regions/bands, single wavelength/color, two wavelength/color or multi-wavelength radiation thermometry are designated. When thermometers' response time is a concern, fast radiation thermometry is denominated. When optical fibers are involved in thermal sensing applications, fiber optic radiation thermometry can be specified. When fluorescent radiation is used in temperature detection, phosphor thermometry is named. These topics are covered in [4, 6-42].

Single wavelength thermometry depends on sensing of the target radiance in a specific spectral region to infer the target temperature. The key problem in single wavelength thermometry is to compensate the unknown target emissivity. Examples are presented in [6-11]. Single wavelength thermometry is widely used in the applications when the target emissivity is known or easy to acquire.

Dual wavelength thermometry samples the target radiance in two different spectral regions and infers a color temperature and/or emissivity using various algorithms. In the case of gray body target, which means the emissivity is independent of the detected wavelength, the temperature can be determined from the ratio of the two signals [3, 12-16]. Brownson et al. [17] have presented a method for determination of the target temperature and emissivity by solving the two detector response equations simultaneously. Ng [18] also demonstrated the working principle of a self calibrating 2-wavelength pyrometer. The pyrometer calibration constant is automatically determined by the pyrometer. The voltage response of detectors at two different wavelengths at many different unknown temperatures was analyzed to determine the calibration constants and used to measure temperatures at subsequent times.

The extrapolation of single/dual wavelength temperature provides us with a general method for determining temperature with multiple wavelength radiation thermometry. Multi-color or multi-wavelength thermometry samples the target radiance in more than two different spectral regions and infers the target temperature and/or emissivity through a variety of algorithms. Sampled spectral wavelengths vary from three [4], six [19], eight [20], to full spectrum (spectrometer) [21]. More and more complex mathematical models are used to

evaluate the temperature and emissivity, varying from linear mathematical correction to artificial neural network estimation [4, 22-26]. A review has been given by Sun et al. [27].

Fast radiation thermometry is used in the applications for measuring high-speed transient temperature (e.g. laser heating of single micro particles [28]). The maximum time resolution of a thermometer is generally limited by the available technical devices such as detectors, amplifiers, and data acquisition [29]. Since there is continuous improvement in these sectors the maximum time resolution of pyrometers has permanently improved [29-30]. In 1976, Ruffino [31] defines high-speed pyrometry as a temperature measurement with a time resolution of the order of a millisecond or less [29]. After two decades, in 1996, Xu et al. [32] developed a monochromatic nanosecond time resolution pyrometer. They mentioned that this was the first time that a nanosecond pyrometer had been described in the literature [29]. A review has been summarized by Mueller et al. [29].

In the context of thermal sensing, fiber optic temperature sensing system dated mostly from the mid to late 1970's. Commercial fabrication began in the early 1980's. Fiber optics for sensor systems can be useful in the presence of a high electrical, magnetic or electromagnetic noise background. The small size of the fiber and its electrical, chemical and thermal inertness allow semi-permanent location of the sensor deep inside complex equipment and thereby provide access to difficult to address locations where temperature may be of interest [33]. At present, it has been widely recognized that various types of sensor can be advantageously made by using optical fiber either as the medium for data transmission or as the sensor transducer, or both. Interested reader can consult the recent publications in the literature [8, 33-37].

Phosphor thermometry utilizes the thermal dependence of phosphor fluorescence to provide for a non-contact, emissivity-independent, optical alternative to other more conventional techniques. Thermographic phosphors are relatively inert, ceramics materials activated with a rare material which emit light with a distinctive spectral distribution when suitably excited by an energy source such as an electron beam, x-ray source, or ultraviolet light. If the source is pulsed, then the fluorescence emitted will persist for a characteristic duration that is temperature dependent. Different spectral components from the same material may even exhibit different temperature responses. These changes are independent of the emissivity of the surface to which the fluorescing material is attached [38, 39]. This unique property makes the phosphor thermometry the only useful approach in many applications. Examples are presented in [40-42]. A review, which includes more than two hundred references, has been given by Allison et al. [39].

## **1.2. Overview**

In this study, non-contact remote-sensing radiation thermometry was used in the applications of temperature measurement in ceramics grinding and diesel exhaust aftertreatment filters. Different radiometric methods, including spectrometer (multi-wavelength), one-color (single wavelength) and two-color (two wavelength) methods, were developed for measuring surface temperatures in the two industrial applications. Employing the spectrometer method to measure the grit-workpiece interface temperatures in magnesia-partially-stabilized zirconia (MgO-PSZ) grinding is described in Chapter 2. Both one-color and two-color methods for measuring temperature distribution in diesel exhaust aftertreatment filters are outlined in Chapter 3 and 4. Partial results have also been covered in three journal papers [43 –45].

Grinding temperature measurements in magnesia-partially-stabilized zirconia using infrared spectrometry is summarized in Chapter 2 and [43]. Non-contact infrared-radiation thermometry methods for grinding temperature measurement and thermal effect in ceramics grinding are first reviewed. A brief discussion is given of the phase transformation during MgO-PSZ grinding and the outstanding performance of SiC wheels in PSZ grinding. The thermal hypothesis of high temperature generated at the grit-workpiece interface helping efficient grinding of PSZ is discussed in terms of the thermal conductivity analysis of zirconia, SiC and diamond and the X-ray diffraction observations of zirconia phase transformation. A set of experiments using the spectrometer method to measure grinding temperature has been described and, the temperature analysis method of spectral blackbody curve matching has been presented. The measured high temperature results are outlined and discussed. Simulation calculations for understanding the averaging process of the grinding hot-spot temperature and a cooler surface background temperature are also discussed.

The development of diesel exhaust aftertreatment technology requires accurate temperature profile data on the inner wall surface of diesel exhaust aftertreatment filters. As outlined in Chapter 3 and [44-45], a fiber optic radiation thermometry system was developed for in-situ measurement of the temperature distribution on the channel wall surface in diesel exhaust aftertreatment filters. Components and features of the system, which include the optical fiber, goniometric characteristics of the fiber tip, and infrared sensor, are first introduced. The temperature measurement strategy using the one-color and two-color methods and sensor calibration are then presented. Results of the temperature measurement experiments conducted in a microwave heated filter are analyzed and compared. The



parasitic heating effect on the temperature measurement results caused by high temperature filter wall surface in contact with the fiber body is also discussed.

In Chapter 4, applying infrared thermometry to study the temperature distribution in microwave heating of diesel particulate filters is presented. Temperature measurement tests were conducted in integrated multi-channel fiber optic infrared temperature measurement and microwave heating systems. Silica light-pipes were employed to collect emitted radiation from the inside wall surfaces of Diesel Particulate Filters (DPFs). The radiation from a small and specific region of the inner filter wall surface can be detected. Temperature is calculated by a one-color infrared transducer (Mikron M680). Components and features of the multi-channel fiber optic temperature measurement and microwave heating systems are first introduced. Temperature measurement calibration and validation of filter wall opacity, use of one-color thermometry method, and the filter heating repeatability are subsequently presented. Experimental setup of filter heating and temperature measurement at 36 locations in a DPF is described. Results from the in-situ temperature measurement experiments performed on three DPFs are then analyzed and discussed.

## References

- [1] R.N. Bigelow, P.S. Carlson, A.M., Hunter, and S.R. King, 1996, "Radiation Thermometry," *Proceedings of the 1996 Measurement Science Conference*, Jan. 25-26, Anaheim, CA.
- [2] S. Green, 1995, "Radiation thermometry: An Introduction to Theory, Technology and Techniques," *Measurement and Control*, Vol. 28, No. 8, pp. 238 – 243.
- [3] S. Salvatori, 2001, "Wide-Band Gap Semiconductors for Noncontact Thermometry," *Journal of Vacuum Science and Technology B*, Vol. 19, No. 1, pp. 219 – 223

- [4] D.P. Dewitt and G.D. Nutter, 1989, *Theory and Practice of Radiation Thermometry*, John Wiley & Sons, pp. 1 – 89 and 490 – 493.
- [5] D. Ng, 1996, “A Self Calibrating Emissivity and/or Transmissivity Independent Multi-Wavelength Pyrometer,” NASA Technical Memorandum 107149
- [6] T. Luchi, 1992, “Radiation Thermometry of Low Emissivity Metals Near Room Temperature,” *Temperature, Its Measurement and Control in Science and Industry*, J. F. Schooley (Ed.), the 7th International Temperature Symposium, Toronto, Ontario, Canada, Apr. 28–May 1, 1992, American Institute of Physics, Vol. 6, pp. 865 – 870.
- [7] N. Yamada, and S. Fujimura, 1992, “Radiation Thermometry for Simultaneous Measurement of Temperature and Emissivity,” *Temperature, Its Measurement and Control in Science and Industry*, J. F. Schooley (Ed.), the 7th International Temperature Symposium, Toronto, Ontario, Canada, Apr. 28–May 1, 1992, American Institute of Physics, Vol. 6, pp. 843 – 848.
- [8] R.R. Dils, 1983, “High-Temperature Optical fiber Thermometer,” *Journal of Applied Physics*, Vol. 54, No. 3, pp. 1198 – 1201.
- [9] R.F. Gansman, 1991, “Using Reflection Measurement to Calculate Emissivity for Improved In-Situ Temperature Measurement in Rapid Thermal Processing,” *MS Thesis, North Carolina State University*.
- [10] D.L. Hartsock, R.B. Dinwiddie, J.W. Fash, T. Dalka, G.H. Smith, Y. Yi, and R. Hecht, 2000, “Development of a High Speed System for Temperature Mapping of a Rotating Target,” *Proceedings of SPIE, Thermosense XXII*, Vol. 4020, pp. 2 – 9.
- [11] S. Jiang, 1993, “Effects of the Medium in Radiation Transmitting Path on Single-Band Infrared thermometry,” *Hongwai Jishu/Infrared Technology*, Vol. 15, No. 6, pp. 37 – 40 (in Chinese).
- [12] W. Small IV, P.M. Celliers, L.B. Da Silva, D.L. Matthews, and B.A. Soltz, 1998, “Two-Color Mid-Infrared Thermometer with a Hollow Glass Optical Fiber,” *Applied Optics*, Vol. 37, No. 28, pp. 6677 – 6683.
- [13] O. Eyal and A. Katzir, 1995, “Temperature Measurements Utilizing Two-Bandpass fiber Optic Radiometry,” *Optical Engineering*, Vol. 34, No. 2, pp. 470 – 473.
- [14] Y. Matsui, T. Kamimoto, and S. Matsuoka, 1980, “A Study on the Application of the Two-Color Method to the Measurement of Flame Temperature and Soot Concentration in Diesel Engines,” SAE 800970.

- [15] S. Wahiduzzaman, T. Morel, J. Timar, and D.P. DeWitt, 1987, "Experimental and Analytical Study of Heat Radiation in a Diesel Engine," SAE 870571.
- [16] H.X. Quoc, J-M. Vignon, and M. Brun, 1991, "A New Approach to the Two-Color Method for Determining Local Instantaneous Soot Concentration and Temperature in a DI Diesel Combustion Chamber," SAE 910736.
- [17] J. Brownson, K. Gronokowski, and E. Meade, 1987, "Two-Color Imaging Radiometry for Pyrotechnic Diagnostics," *in selected Papers on Temperature Sensing: Optical Methods*, R.D. Lucier, ed., Vol. MS116 of SPIE Milestone Series (SPIE, Bellingham, Wash.), pp. 525 – 532.
- [18] D. Ng, 1998, "Self Calibration of a 2-Wavelength Pyrometer," NASA/TM 1998-208808.
- [19] A. Cezairliyan, G.M. Foley, M.S. Morse, and A.P. Miller, 1992, "Six-Wavelength Millisecond-Resolution Pyrometer," *Temperature, Its Measurement and Control in Science and Industry*, J. F. Schooley (Ed.), the 7th International Temperature Symposium, Toronto, Ontario, Canada, Apr. 28–May 1, 1992, American Institute of Physics, Vol. 6, pp. 757 – 762.
- [20] X. Sun, X. Hu, j. Dai, and D. Cong, 2001, "Eight-Wavelength Pyrometer Which can simultaneously Measure the True Temperature and Spectral Emissivity," *Guangxue Jishu/Optical Technique*, Vol. 27, No. 4, pp. 305 – 306 & 309 (in Chinese).
- [21] D. Ng, "Temperature Measurement Involving Nanostructured Thermal Barrier Coating Using a Multiwavelength Pyrometer," NASA Technical Memorandum 107286.
- [22] R.A. Felice, 1998, "Temperature Determining Device and Process," US Patent, No. 5,772,323.
- [23] D. Ng, 1996, "A Self Calibrating Emissivity and/or Transmissivity Independent Multi-Wavelength Pyrometer," NASA technical Memorandum, 107149.
- [24] D. Ng, 1996, "Application of the Self Calibrating Emissivity and/or Transmissivity Independent Multi-Wavelength Pyrometer to Measure the Temperatures of Tungsten and Refractory Material Surfaces," NASA technical Memorandum, 107152.
- [25] G.B. Hunter, C. Allemand, and T.W. Eagar, 1985, "Multiwavelength Pyrometer – An Improved Method," *Optical Engineering*, Vol. 24, No. 6, pp. 1081 – 1085.

- [26] D. Cong, J. He, J. Dai, X. Sun, and Z. Chu, 2000, ‘Theoretical Study of Multi-Wavelength Radiation Thermometry Based on RBF Neural Network,’ *Yi Qi Yi Biao Xue Bao/Chinese Journal of Scientific Instrument*, Vol. 21, No. 5, pp. 480 – 484.
- [27] X. Sun, C. Li, J. Dai, and Z. Chu, “Review on the Theory of Multi-Spectral Radiation Thermometry,” *Jiliang Xuebao/Acta metrological Sinica*, Vol. 23, No. 4, pp. 248 – 250 & 286 (in Chinese).
- [28] W. Maswadeh, A. Tripathi, N.S. Arnold, J. DuBow, and Henk L.C. Meuzelaar, 1994, “High speed, Two-Wavelength Radiation Thermometry of Single Micro Particles during CO<sub>2</sub> Laser Heating,” *Journal of Analytical and Applied Pyrolysis*, Vol. 28, No. 1, pp. 55 – 70.
- [29] B. Mueller, and U. Renz, 2001, “Time Resolution Enhancement of a Fiber-Optic Two-color Pyrometer,” *Proceedings of SPIE, Thermosense XXIII*, Vol. 4360, pp. 447 – 454.
- [30] F. Righini, G.C. Bussolino, and A. Rosso, 1992, “Trends in High-Speed pyrometry at IMGC,” *Temperature, Its Measurement and Control in Science and Industry*, J. F. Schooley (Ed.), the 7th International Temperature Symposium, Toronto, Ontario, Canada, Apr. 28–May 1, 1992, American Institute of Physics, Vol. 6, pp. 763 – 768.
- [31] G. Ruffino, 1976, “High-Speed Radiation Pyrometry,” *High Temperatures – High Pressures*, Vol. 8, pp. 143 – 154.
- [32] X. Xu, C.P. Grigoropoulos, and R.E. Russo, 1996, “Nanosecond-Time-Resolution Thermal Emission Measurement during Pulsed Excimer-Laser Interaction with Materials,” *Applied Physics A: Materials Science & Processing*, Vol. 62, No. 1, pp. 51 – 59.
- [33] K.A. Wickersheim, 1992, “Fiberoptic Thermometry: An Overview,” *Temperature, Its Measurement and Control in Science and Industry*, J. F. Schooley (Ed.), the 7th International Temperature Symposium, Toronto, Ontario, Canada, Apr. 28–May 1, 1992, American Institute of Physics, Vol. 6, pp. 711 – 714.
- [34] B.E. Adams, 1992, “Optical Fiber Thermometry for Use at High temperatures,” *Temperature, Its Measurement and Control in Science and Industry*, J. F. Schooley (Ed.), the 7th International Temperature Symposium, Toronto, Ontario, Canada, Apr. 28–May 1, 1992, American Institute of Physics, Vol. 6, pp. 739 –743.
- [35] M. Gottlieb and G.B. Brandt, 1981, “fiber-Optic Temperature Sensor Based on Internally Generated Thermal Radiation,” *Applied Optics*, Vol. 20, No. 19, pp. 3408 – 3414.

- [36] A. Wang, S. Gollapudi, R.G. May, K.A. Murphy, and R.O. Claus, 1995, "Sapphire Optical Fiber-Based Interferometer for high Temperature Environmental Applications," *Smart Mater. Struct.*, Vol. 4, pp. 147 – 151.
- [37] X. Fang, R.G. May, A. Wang, R.O. Claus, 1994, "A Fiber-Optic High-Temperature Sensor," *Sensors and Actuators A*, Vol. 44, pp. 19 – 24.
- [38] D.L. Beshears, R.A. Abston, S.W. Allison, W.H. Andrews, M.R. Cates, E.B. Grann, W.W. Manges, T.J. McIntyre, M.B. Scudiere, M.L. Simpson, D.N. Sitter, J. Vehec, and L. Zhang, 1997, "Application of Phosphor Thermometry to galvanneal Processing," *Instrumentation in the Aerospace Industry: Proceedings of the International Symposium*, Vol. 43, pp. 795 – 800.
- [39] S.W. Allison, and G.T. Gillies, 1997, "Remote Thermometry with Thermographic Phosphors: Instrumentation and Applications," *Review of Scientific Instruments*, Vol. 68, No. 7, pp. 2615 – 2650.
- [40] K.W. Tobin, S.W. Allison, M.R. Cates, G.J. Capps, D.L. Beshears, M. Cyr, and B.W. Noel, 1990, "High-Temperature Phosphor Thermometry of Rotating Turbine Blades," *AIAA Journal*, Vol. 28, No. 8, pp. 1485 – 1490.
- [41] W.W. Manges, S.W. Allison, J.R. Vehec, "Galvanneal Thermometry with a Thermographic Phosphor System," *Iron and Steel Engineer*, Vol. 74, No. 12, pp. 34 – 36.
- [42] W. Vander, L. Randall, P.A. Householder, and T.W. II Wright, 1999, "Phosphor Thermometry in Combustion Applications," *Applied Spectroscopy*, Vol. 53, No. 10, pp. 1251 – 1258.
- [43] A.C. Curry, A.J. Shih, R.O. Scattergood, J. Kong, and S.B. McSpadden, 2003, "Grinding Temperature Measurements in MgO PSZ Using Infrared Spectrometry," *J. Am. Ceram. Soc.*, Vol. 86, No. 2, pp. 333 – 341.
- [44] B.J. Boothe, A.J. Shih, J. Kong, and W.L. Roberts, 2003, "Goniometric Characteristics of Optical Fibres for Temperature Measurement in Diesel Engine Exhaust Filters," *Measurement Science and Technology*, Vol. 14, No. 5, pp. 563 – 572.
- [45] J. Kong and A.J. Shih, "Infrared Thermometry for Diesel Exhaust Aftertreatment Filter Temperature Measurement," SAE Transactions (submitted)

## CHAPTER 2. GRINDING TEMPERATURE MEASUREMENTS IN MGO-PSZ USING INFRARED SPECTROMETRY

### 2.1. Introduction

Heat generation is an important factor for the grinding of ceramics. It can degrade the integrity of the wheel matrix and/or abrasive; reduce workpiece surface quality by causing thermal cracks or burning of the surface; introduce strength-reducing tensile residual stresses; and create dimensional inaccuracies. Temperature may also influence the grinding mechanism, either by softening the material or by introducing phase transformations [1–3].

Although thermocouples are ideal for many temperature-measurement applications, they are severely limited for measuring grinding temperatures. Their shortcomings lie in their poor spatial and temporal resolutions. Resolution is dictated by the size of the hot junction, time response of the thermocouple, and the conductivity through the workpiece. Furthermore, the low thermal conductivity of ceramics requires any contacting temperature measurement device be placed so close to the grinding zone that it will likely be destroyed before an accurate temperature can be obtained. These difficulties make non-contact fast time-response methods, such as infrared emission spectroscopy, more suitable for grinding temperature measurement.

A number of researchers have undertaken the task of determining the temperatures generated during grinding. The majority of temperature measurement methods reported to date can be divided into the following categories: “blind-hole”, “through-hole”, “wheel-surface”, and “grinding-interface”. In assessing the different methods, it is important to note

the difference between single-wavelength and multiple-wavelength methods. So-called "single-wavelength" methods measure the intensity of the spectral output without discriminating between different wavelengths. Calibration techniques are needed so that the absolute value of the measured intensity can be correlated with source temperature. This requires knowledge of the emissivity of the source as well as all other parameters that modify intensity between source and detector. In contrast, so-called "multiple-wavelength" techniques use the ratio of two or three intensities at specific wavelengths to determine temperature in conjunction with blackbody radiation curves. As long as emissivity and other parameters are independent of wavelength over the measurement range, these do not have to be determined independently. Spectrometer methods determine the intensity spectrum from the source over a wavelength range and fit this to blackbody curves to determine temperature, again assuming that all relevant parameters are independent of wavelength. Spectrometer methods have the advantage that spurious effects such as tribo-luminescence peaks should be detectable in the spectral output.

Blind-hole methods [4–6] involve measurement of the temperature below the grinding surface. This is done by monitoring the temperature at the upper surface of a blind hole drilled into the workpiece from the bottom. Temperature is monitored as the distance from the measured surface to the grinding surface decreases with subsequent passes of the wheel. Until the distance of the measurement from the grinding surface is very small, approximately on the order of the distance between individual grinding grits, conduction effects dictate that the temperature of individual grits cannot be resolved. Extrapolated temperatures represent an uncertain average value. Through-hole methods [7–9] involve the observation of radiation emitted by the wheel and passing through a hole in the workpiece.

Depending on the geometry and the type of measurement method used, peak temperatures can be measured. Peak temperatures from individual asperity contacts have been determined using high spatial resolution detectors [7]. The wheel-surface method [10] provides wheel temperatures at various points about the grinding wheel periphery. An average surface temperature is measured in this case. With the grinding-interface methods, temperatures are measured within the grinding zone and at asperity contacts in pin-on-disk rubbing. The grinding study presented by Outwater and Shaw [11] employs a thermocouple method in which dissimilar metals are smeared across the grinding surface by the wheel. This method, which provides the average temperature across the smeared region, does not measure hot-spot temperatures. Chandrasekar and coworkers [7,9] and Griffioen, et al. [12] have developed grinding-interface methods pertinent to this study. In their studies, asperity peak temperatures were estimated for single-point cutting/sliding or full-wheel grinding. The infrared transmission through a transparent workpiece was used for the measurements reported by Griffioen, et al. [12].

## **2.2. Thermal effects in grinding**

The grinding process is best understood by considering it on global and local scales. Distinctions between the two are particularly important in discussing grinding temperature. When a grinding grit engages the workpiece, it first causes deformation. This stage is known as plowing. If the stress level becomes great enough, chip formation begins. Finally, the chip breaks loose and is carried out of the grinding zone by grinding fluid. The fluid serves both to remove chips, collectively known as swarf, and to cool the workpiece. Cooling is often critical in grinding because a significant amount of heat is typically generated in the



process. Heat is generated primarily by three actions. First is shearing or fracture of the workpiece during chip formation. Second is the friction of the chip sliding at the grit's rake face. Lastly, heat is generated along the portion of the grit worn flat either by truing or by previous passes through the workpiece. Heat generated by any of these means, when it is localized near the grit or in the chip, is known as hot-spot (flash) temperature. Each grit acts as an asperity heat source, with conduction serving to distribute the heat from individual grits and raise the overall temperature of the grinding surface [5,7]. The temperature far from the grits is known as the background temperature. As would be expected, and as some researchers have shown, the values of these temperatures typically differ substantially, especially in materials with low thermal conductivity, such as ceramics.

The defining characteristic of transformation-toughened ceramics, such as the partially stabilized 9 mol% MgO Partially Stabilized Zirconia (MgO-PSZ) used for this study, is the introduction of a metastable phase. The effects occurring during grinding can be viewed in terms of the MgO-PSZ phase diagram shown in Fig. 2.1. After appropriate heat treatment [13], the cubic (c), monoclinic (m), and tetragonal (t) phases are present at room temperature. The c and t phases are metastable at room temperature. Stress will drive the  $t \rightarrow m$  martensitic transformation that increases toughness. Increasing temperature can also transform both c and t phases to the stable m phase. Above 1513 K (1240 C) the m phase will become unstable, and at even higher temperatures only c and liquid phases will be stable. The thermomechanical history during grinding is complex since there will be a rapid increase in both stress and temperature at the grit-workpiece interface followed by a rapid quench in grinding coolant. Analysis of the phases present before and after grinding, in both chips and ground surfaces, gives some indication of the history. However, the picture is limited since

conventional x-ray diffraction techniques can distinguish the amount of m phase and c + t phases present, but not the individual amounts of the c and t phases.

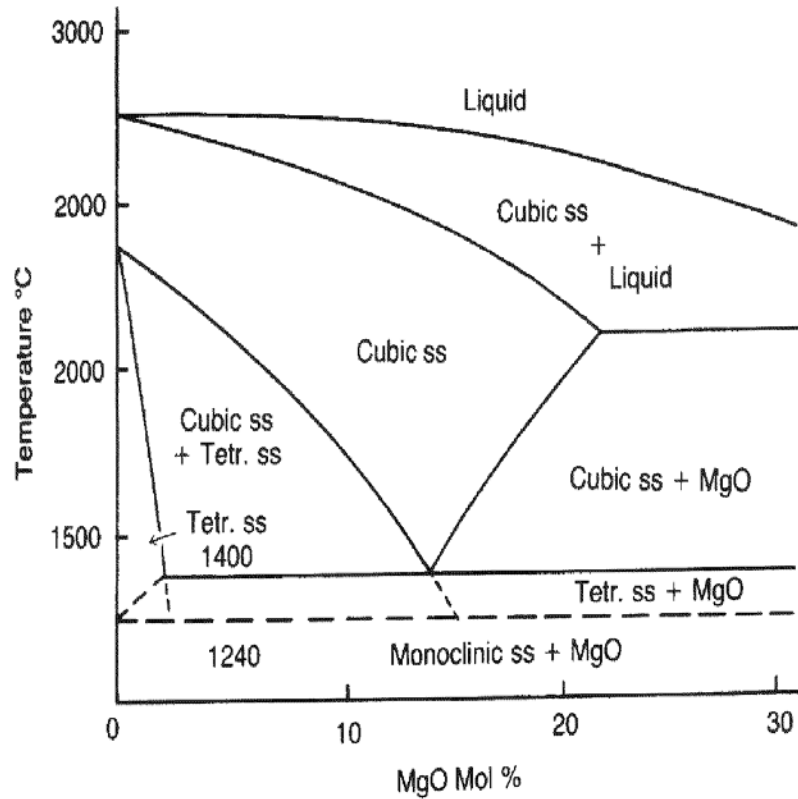


**Figure 2.1. Phase diagram for MgO-PSZ [19].**

The grinding performance of the PSZ material used in this study was investigated in detail in a several companion studies [14–16]. SiC and diamond-grinding wheels were used on two different machines for a systematic investigation of grinding behavior. When the grinding wheel specifications are properly chosen, a SiC grinding wheel performs remarkably well for grinding PSZ. Diamond grinding wheels have been the traditional choice for these and most other structural ceramics. Rather surprisingly, the highest G-ratios are obtained at higher grinding rates for the SiC wheel. This, and the fact that SiC grinding

wheels can be readily shaped for use in precision cylindrical form grinding, has been exploited for cost-effective production of PSZ components in automotive applications. Several important effects were noted in the companion study. X-ray diffraction showed that the m phase was not present in any of the grinding chips when SiC wheels were used. Some m phase was retained in the chips with diamond wheels. In contrast, the ground surfaces contained excess, relative to virgin surfaces, of the m phase. Thermal conductivity must play a role in these effects. The thermal conductivity is approximately 2, 150, and 2000  $\text{Wm}^{-1}\text{K}^{-1}$  for zirconia, SiC, and diamond, respectively. Very low thermal conductivity for zirconia will help retain heat and raise temperature, especially in grinding chips, which have restricted volume. High chip temperatures, as well as stresses, would modify the phases present after grinding. High temperatures at the grit-workpiece interfaces could also locally soften or even partially melt the PSZ. These issues motivated the current investigation for the determination of grinding temperatures using PSZ workpieces with SiC and diamond wheels. An advantage of PSZ is the fact that it is semi-transparent in the near infrared and light transmitted through the workpiece can be collected. For the method implemented here, it was possible to make measurements in the presence of grinding coolant, so that the results reflect the conditions present in real grinding processes.

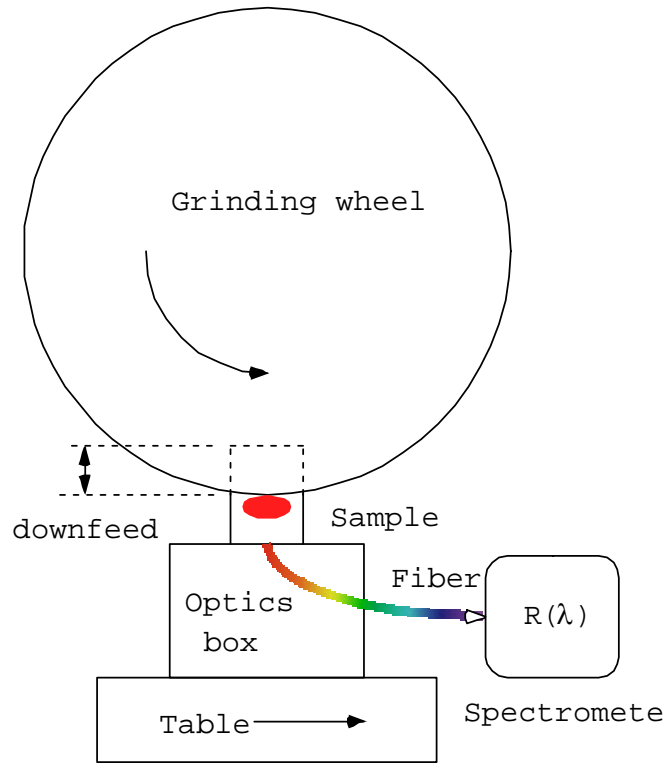
Several previous studies support the hypothesis for high temperatures at the grit-workpiece interface during grinding of zirconia. Using a three-wavelength technique, Hebbar et al. [7] reported single-point and full-wheel peak temperatures in the order of 1600 to 1900 K for zirconia. In their studies of abrasive behavior of zirconia, Costa et al. [2], and Swain and Hannink [3] report that the temperature generated during abrasive processes can counteract the stress-induced transformation,  $t \rightarrow m$ , by producing the reverse

transformation  $m \rightarrow t$  above 1513 K (Fig. 2.1). Swain and Hannink [3] also note that the temperatures at the interface in grinding should be substantially elevated due to the low thermal conductivity of zirconia. Although zirconia was not tested, Griffioen, et al. [12] used an infrared camera transmission technique and reported peak temperatures as high as 3000 K for single-point contacts of silicon nitride pins sliding on transparent sapphire workpiece.

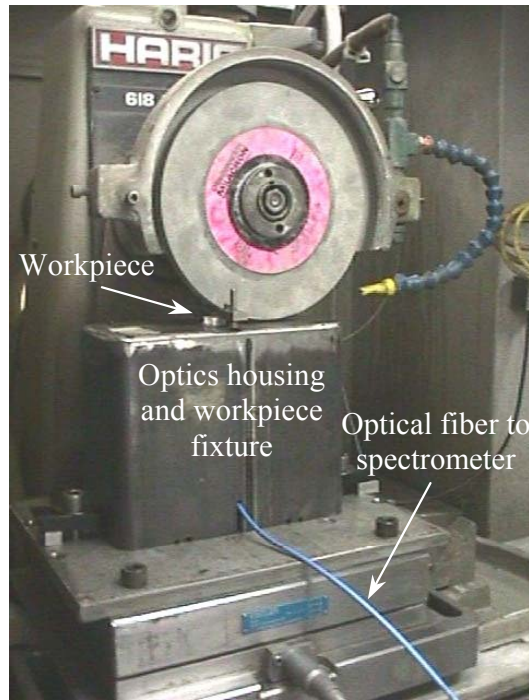
### 2.3. Experimental Procedure

Grinding tests were done on a Harig surface grinder. The table speed was fixed at 150 mm/s. The wheel speeds used were 3500, 4000, and 4500 rpm (37, 42, and 47 m/s surface cutting speed, respectively). Downfeeds, i.e., nominal depths of cut (Fig. 2.2(a)), were 0.0025, 0.005, and 0.0075 mm. Specimen thickness depended on the number of prior grinding passes, and these varied from about 0.1 to 1.3 mm. Two grinding wheels were used. The first was a specially selected 220 ANSI mesh SiC grit vitreous bond wheel [16] while the second was a 220 ANSI mesh diamond grit resin bond wheel. Both wheels measured 200 mm in diameter with a width of 10 mm. Water-based Cimtech 500 synthetic coolant at 5 % concentration was used during grinding. Sample fixturing and other details of the grinding procedure are given in [15]. The workpiece material used for all grinding tests was 9 mol % MgO-PSZ supplied by Coors.

**Figure 2.2. (a) Schematic of the grinding test setup and (b) Photograph of the setup.**



(a)



(b)

Temperature measurements were conducted with two different spectrometers. All of the test results reported here were obtained using an Ocean Optics USB2000 near-infrared (0.717 to 0.980  $\mu\text{m}$  wavelength range) spectrometer. For comparison, selected tests were also done using an Ocean Optics S2000 visible (0.191 to 0.853  $\mu\text{m}$  wavelength range) spectrometer. Ocean Optics' spectrometers take advantage of charge-coupled discharge (CCD) arrays to allow for acquisition of an entire spectrum over one sampling time. Furthermore, they are relatively inexpensive and can be readily integrated with a data acquisition system. As seen in the schematic of the test setup in Fig. 2.2(a), light transmitted through the PSZ workpiece is collected and fed to a 600  $\mu\text{m}$  diameter multi-mode optical fiber which is carried to the spectrometer aperture for intensity measurements. A common problem in using optical fibers for temperature measurement is the signal attenuation that can result from changes in the fiber's orientation. However, as long as there is no spectral variation in the attenuation, it does not affect the spectrometric measurement method used here. Furthermore, when a steady source was used to check the fibers for signal attenuation due to movement of the fiber, none was observed. The actual test setup implemented on the grinding machine is shown in Fig. 2.2(b). The cable running from the optics housing passes the light to the spectrometer (not shown). The measurement signal can only be captured when the moving workpiece on the table passes under the grinding wheel (Fig. 2.2(a)), therefore the measurement-time window is limited by the grinding table speed (150 mm/s) and sample size (20 x 20 x 6.35 mm). Typical data collection times were the order of 60 ms or less.

The spectrometers must first be calibrated to a known temperature source to obtain accurate spectra. Calibrating the spectrometer sets each pixel in its CCD array to the

appropriate gain. This ensures that the relative intensities of each wavelength are correct, so the spectra shapes accurately indicate the source temperatures. Three sources were used for initial calibration and for verification of the calibrations: a tungsten halogen lamp at 3100 K and blackbody ovens at 1273 and 2773 K. Spatial resolution of the system shown in Fig. 2.2 was insufficient to resolve individual grinding grits, therefore, the field of view will contain multiple grinding grit contacts (hot spots) distributed over a background, like stars in a night sky. As will be discussed further, the temperatures measured using the spectrometer method must be interpreted with the aid of simulations.

#### **2.4. Analysis Method and Results**

Multiple-wavelength techniques use relative intensities at different wavelengths to determine an effective (graybody) source temperature. For the spectrometer method used here, this was done by matching the scaled spectrometer output,  $R(\lambda)$ , to blackbody curves,  $E_B(\lambda, T)$ , over the measurement wavelength range. This is illustrated schematically in Fig. 2.3. The  $R(\lambda)$  data is scaled (shifted vertically) and simultaneously matched with  $E_B(\lambda, T)$  curves until the best fit with one of the blackbody curves is obtained. For example, in Fig. 2.3 the output  $R(\lambda)$ , taken over the measurement range  $1 \mu\text{m} \leq \lambda \leq 2 \mu\text{m}$ , fits best to the 2000 K blackbody curve using a scaling factor of 0.3. The effective graybody source temperature determined from the  $R(\lambda)$  spectrum is thus 2000 K.



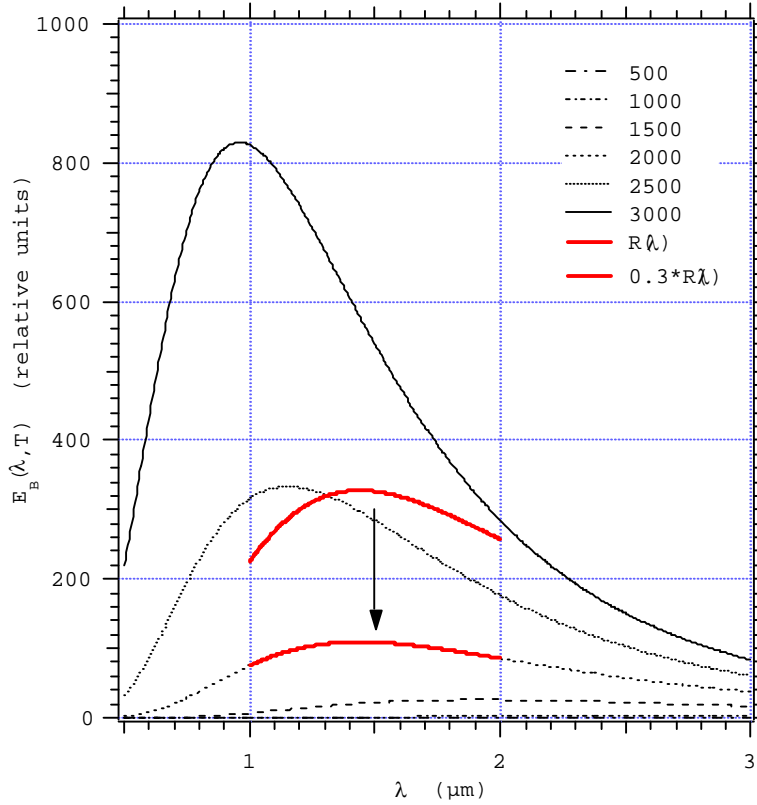


**Figure 2.3. Blackbody radiation curves for the temperatures indicated. Scaling (vertical shift) of the  $R(\lambda)$  spectral data produces a best fit for 2000 K, as indicated.**

The equation used for the data analysis method is based on the blackbody radiation equation plotted in Fig. 2.3,

$$E_B(\lambda, T) = \frac{c_1}{\lambda^5 \left( e^{\frac{c_2}{\lambda T}} - 1 \right)} \quad (2.1)$$

$C_1 = 8\pi hc = 4.992 \times 10^{-24} \text{ Nm}^2$  and  $C_2 = hc/k = 14390 \text{ } \mu\text{mK}$  where  $h$ ,  $k$ , and  $c$  are Planck's constant, Boltzmann's constant and the velocity of light, respectively. For radiation at temperature  $T$  from a source of emissivity  $\varepsilon$  passing through a material with transmissivity

$\tau$  into a spectrometer with an aperture constant  $\alpha$ , the spectrometer output function  $R(\lambda)$  would be the graybody spectrum

$$R(\lambda) = \frac{\alpha \varepsilon \tau C_1}{\lambda^5 \left( e^{\frac{C_2}{\lambda T}} - 1 \right)} \quad (2.2)$$

Assuming that the constants  $\varepsilon$ ,  $\tau$ , and  $\alpha$  are independent of wavelength over the measurement range, a scaled spectrometer output function based on Eq. (2.2) can be written as

$$SR(\lambda) = E(\lambda, T) = \frac{1}{\lambda^5 \left( e^{\frac{C_2}{\lambda T}} - 1 \right)} \quad (2.3)$$

$S$  is the adjustable scale factor accounting for the unknown constants. For source temperatures less than about 3000 K and wavelengths less than 1  $\mu\text{m}$ , the following approximation is valid since the term  $\exp(-C_2/\lambda T) \ll 1$ .

$$SR(\lambda) = E(\lambda, T) = \frac{e^{-\frac{C_2}{\lambda T}}}{\lambda^5 \left( 1 - e^{-\frac{C_2}{\lambda T}} \right)} \cong \frac{e^{-\frac{C_2}{\lambda T}}}{\lambda^5} \quad (2.4)$$

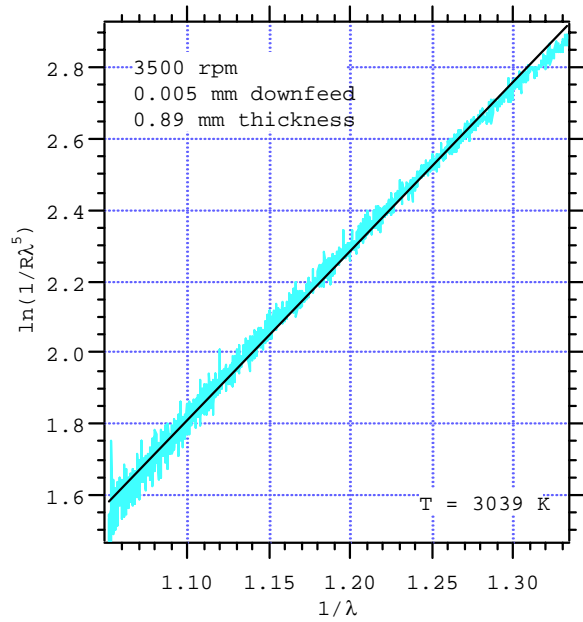
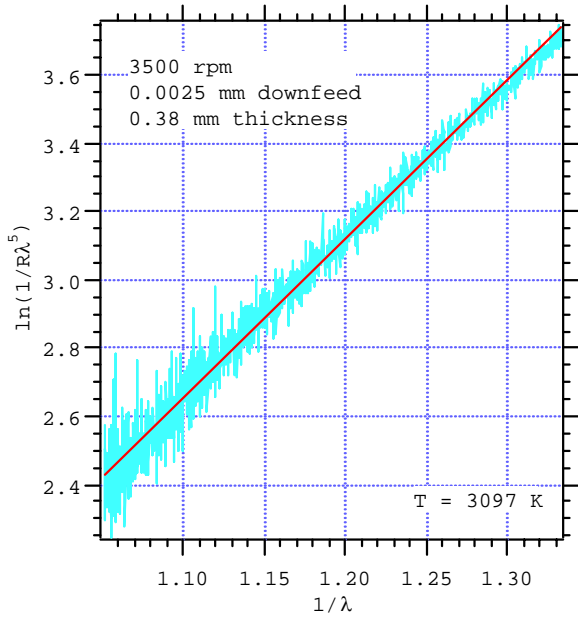
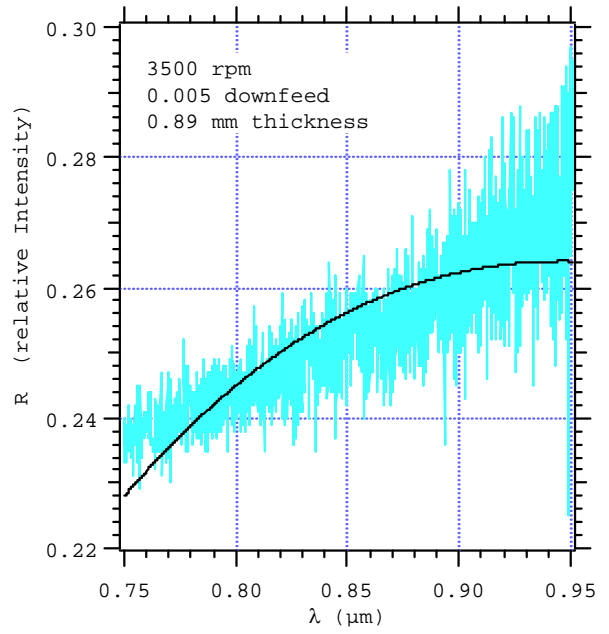
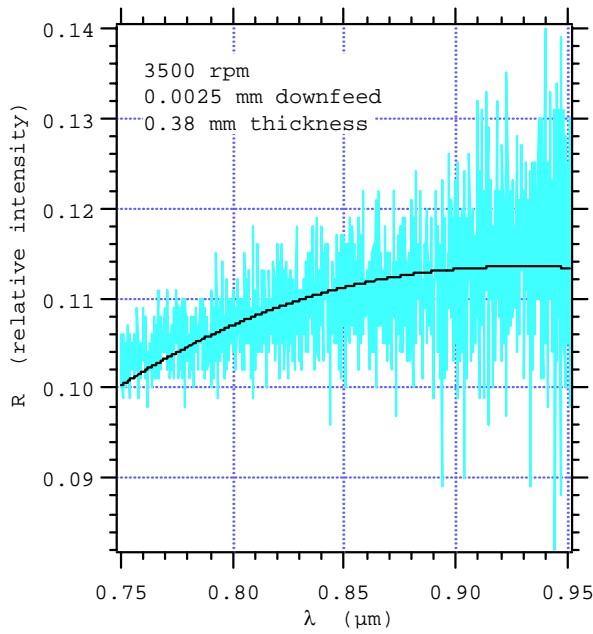
Taking natural logarithms of both sides of Eq. (2.4) and rearranging gives

$$\ln\left(\frac{1}{\lambda^5 R(\lambda)}\right) = \frac{C_2}{T} \frac{1}{\lambda} + \ln S \quad (2.5)$$

Equation (2.5) is the basis of the data analysis method used here. For a spectrometer measurement function,  $R(\lambda)$ , a plot of  $\ln(1/\lambda^5 R)$  vs.  $1/\lambda$  should be a straight line. Using a linear least-squares fit over the near-infrared wavelength measurement range adopted for the tests,  $0.75 \mu\text{m} \leq \lambda \leq 0.95 \mu\text{m}$ , the temperature  $T$  and scale factor  $S$  can be obtained from the slope and intercept, respectively. Alternatively, both sides of Eq. (2.5) can be multiplied by  $\lambda$  and the identification of the slope and intercept will be interchanged. This equivalent equation was proposed by Ng, et al. [17,18] for temperature analysis using a multi-wave pyrometer.

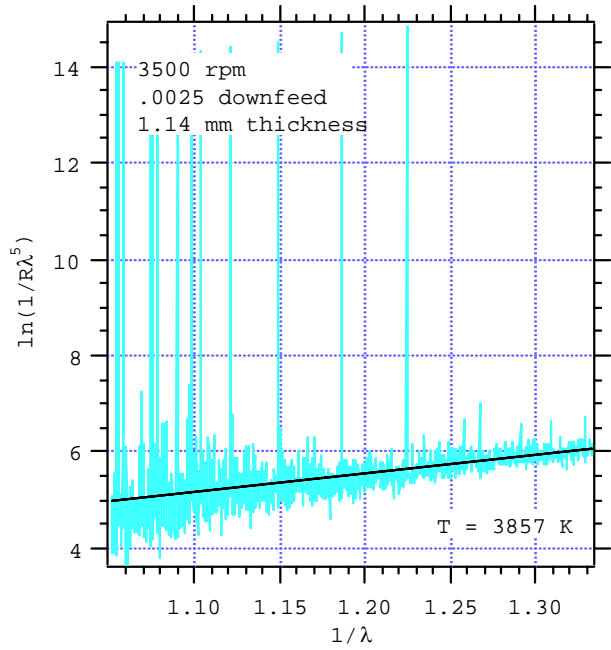
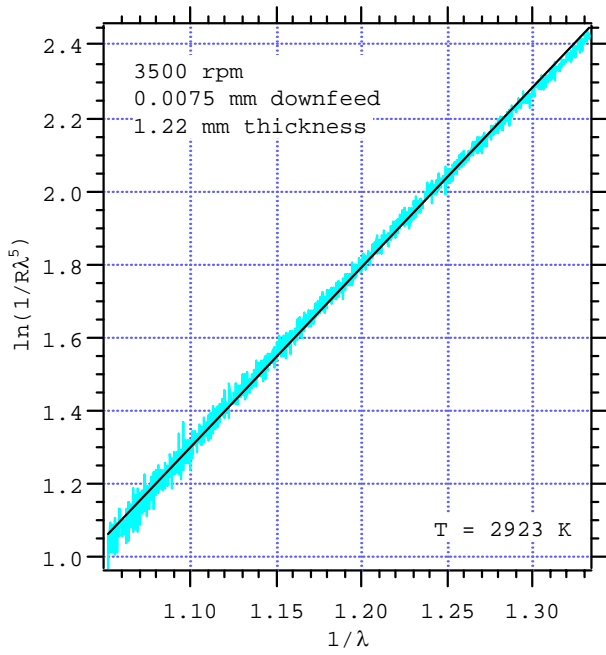
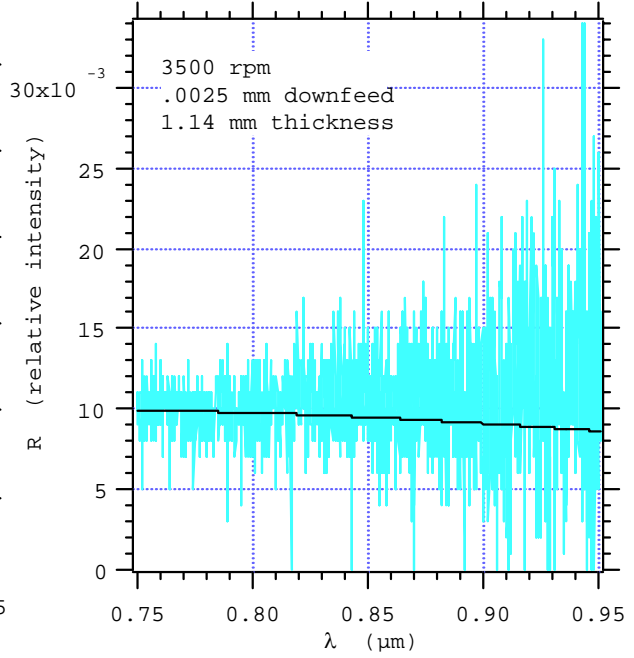
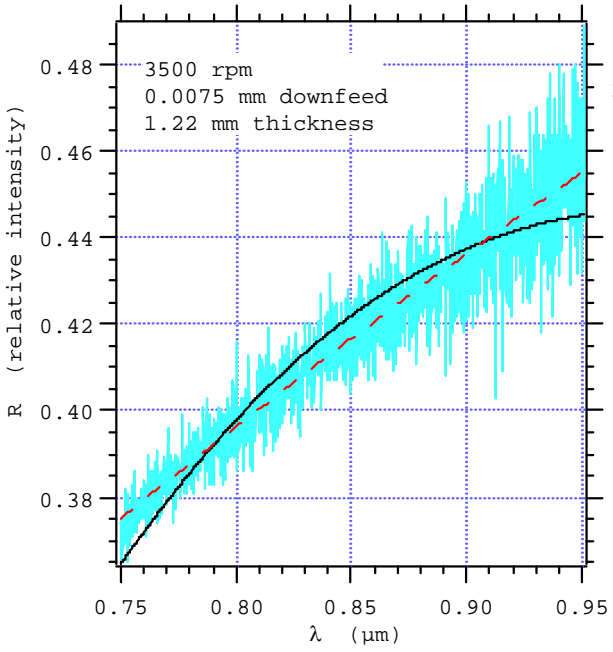
Figures 2.4(a)–2.4(c) show the near-infrared range spectrometer data taken for SiC-ground PSZ at increasing grinding downfeeds. The top frame in each plot is the spectrometer output function,  $R(\lambda)$ , for the grinding conditions indicated while the bottom frame shows the least-squares fit (solid line) according to Eq. (2.5). The solid curve through the  $R(\lambda)$  plot is the fitted blackbody curve for the temperature and scale factor determined. Similar plots were obtained for other grinding conditions used in this study. The results for the source temperatures are summarized in Table I. Since no physical significance can be attached to the scale factors, these are not shown. For a given set of grinding conditions, the four to five temperature values reported in Table I correspond to grinding PSZ workpieces with different thickness.

**Figure 2.4. Top frame shows the measured spectrometer output,  $R(\lambda)$  vs.  $\lambda$ , and the best-fit blackbody curve (solid line). Bottom frame shows the least-squares fit (solid-line) and effective temperature obtained using Eq. (2.5). Wheel speed, downfeed and sample thickness are indicated for each test. (a)-(c) SiC grinding wheel and (d) Diamond grinding wheel.**



(a)

(b)



(c)

(d)

**Table 2.1. Summary of the results for the temperature measurements. Grinding conditions given: Wheel rpm (Speed), downfeed (Feed), material removal rate per mm of wheel width (MRR). The grinding table speed was 150 mm/s for all tests.**

### SiC Grinding Wheel Temperatures

Speed rpm)	3500	3500	3500	4000	4500
Feed (mm)	.0025	.005	.0075	.005	.005
MRR (mm <sup>2</sup> /s)	.375	.75	1.125	.75	.75
T (°K)	3094	3014	2923	3007	2952
	3095	3039	2970	3035	3013
	3069	3062	2972	3022	3020
	3097	3063	2956	3023	3003
		*		3007	3008
Average	<b>3089</b>	<b>3045</b>	<b>2955</b>	<b>3019</b>	<b>2999</b>
Deviation	<b>13.2</b>	<b>23.2</b>	<b>22.6</b>	<b>11.9</b>	<b>27.1</b>

\* One test result gave a value of 2558 K. This appeared spurious and is not included in the average.

### Diamond Grinding Wheel Temperatures

Speed (rpm)	3500	3500	3500
Feed (mm)	.0025	.005	.0075
MRR (mm <sup>2</sup> /s)	.375	.75	1.125
T (°K)	3429	3191	2963
	3203	3021	2951
	3857	2969	2939
	3507	3060	2943
	3035		
Average	<b>3406**</b>	<b>3060</b>	<b>2949</b>
Deviation	<b>313.4</b>	<b>94.8</b>	<b>10.6</b>

\*\* Signal strength was weak and scatter in the data for these grinding conditions was large

The average temperatures in Table 2.1 are on the order of 3000 K for all conditions. No major trends for the effect of grinding conditions on the temperature can be identified. There does appear to be a slight decrease in temperature when downfeed is increased at constant wheel speed (SiC and diamond wheels) or when wheel speed is increased at constant downfeed (SiC wheel). However, these changes are close to the measurement standard deviations. There was a

large amount of scatter in the data for the diamond wheel at the lowest downfeed, 0.0025 mm. The intensities measured were weak in this case and there was considerable scatter in the spectral outputs. Fig. 2.4(d) shows typical results for 0.0025 mm downfeed diamond grinding tests.

If the wavelengths or source temperatures are higher than those assumed for the approximation given in Eq. (2.4), the method based on Eq. (2.5) may not be valid. Nevertheless, the same general approach for temperature measurement can be used. The difference is that one can no longer use the linear form given in Eq. (2.5) for the data fit, and a non-linear regression method must be used. A method for this is outlined in the Appendix.

## 2.5. Discussion

A number of important features emerge from the results presented here. First, the source temperature results shown in Table I were consistent when selected measurements were repeated using the visible (Ocean Optics S2000) spectrometer over the range  $0.4 \mu\text{m} \leq \lambda \leq 0.8 \mu\text{m}$  [15]. This gives us confidence that the temperatures measured are due to thermal sources as opposed to a tribo-luminescent source. The latter is expected to produce localized peaks somewhere in the spectral output. If these did occur in one or the other of the spectrometer measurement ranges, then evidence of this would be apparent in the spectral outputs, and the temperature values reported in Table I should also show corresponding variations. This was not observed.

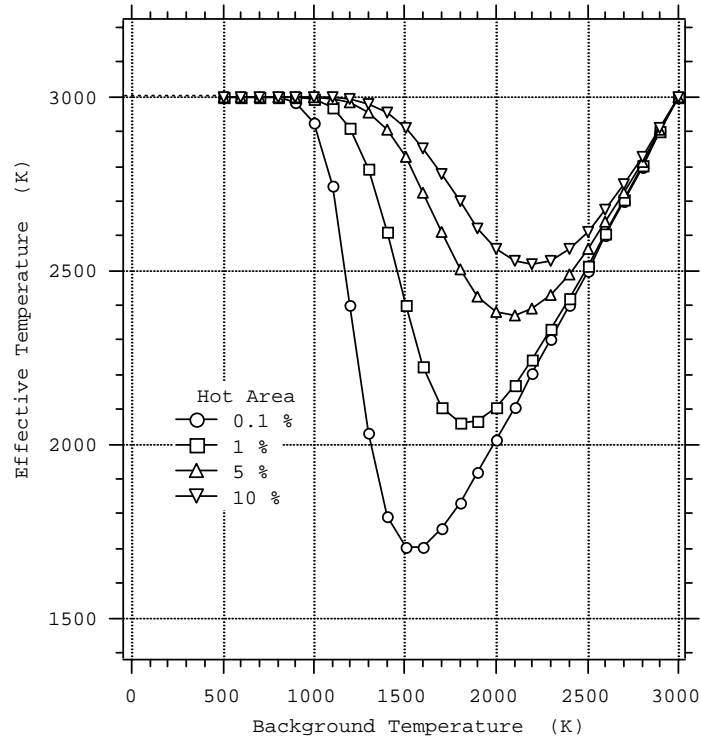
The estimation of temperature based on Eq. (2.5), or the Appendix, produces an effective graybody source temperature defined by matching the measured spectrometer output spectra to blackbody curves over the wavelength measurement range. The scaling constant,  $S$ , and temperature,  $T$ , are adjustable parameters that provide the best least-squares regression fit. If a distribution of temperature exists within the source, then the effective temperature represents an



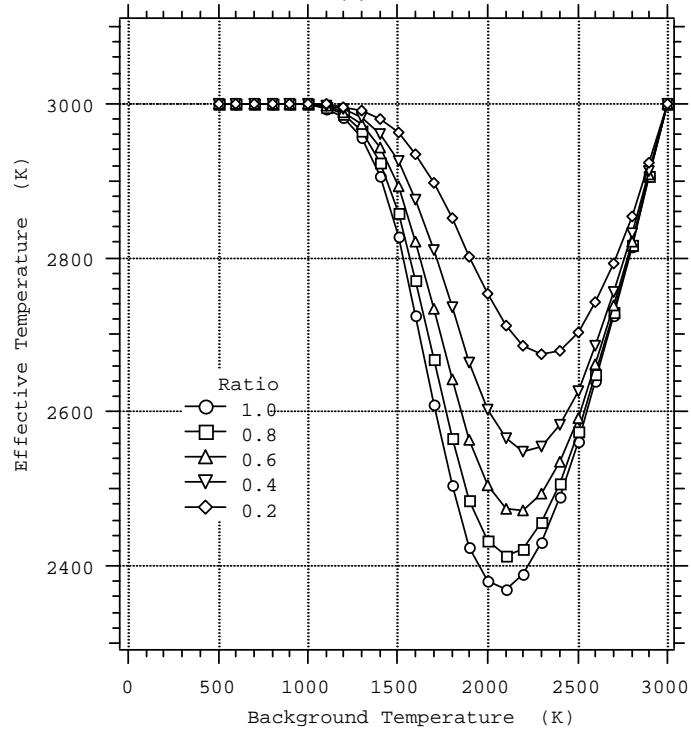
average over this distribution. Because of the non-linear dependence of the blackbody curves on temperature shown in Fig. 2.3, the averaging process will be biased with respect to temperature. The nature of this averaging process for grinding can be understood by using simulation calculations. Because of the localized contacts between grinding grits and workpiece material, there will be a distribution of grinding hot-spots within the aperture of the spectrometer field-of-view. During the duration of a measurement, the hot-spot distribution varies in both spatial and time coordinates. It will be sufficient to consider a time-average, bimodal spatial variation of temperature such that, within the aperture, there is an area fraction  $f_h$  of hot-spot temperature,  $T_h$ , combined with an area fraction,  $1 - f_h$ , of temperature  $T_b \leq T_h$ , i.e., a cooler surface background temperature. The spectral power density received within the spectrometer aperture will then be proportional to the area-average function

$$E_{\text{avg}}(\lambda) = \varepsilon_h f_h E(\lambda, T_h) + \varepsilon_b (1 - f_h) E(\lambda, T_b) \quad (2.6)$$

where  $E(\lambda, T)$  is given by Eq. (2.3).  $\varepsilon_h$  and  $\varepsilon_b$  are the hot spot and background emissivity, respectively (assumed to be independent of  $\lambda$ ). In order to determine an effective temperature,  $T$ , for this simulated distribution, set  $R(\lambda) = E_{\text{avg}}(T)$  for specified values of  $T_h$ ,  $f_h$ ,  $T_b$ ,  $\varepsilon_h$ , and  $\varepsilon_b$ , then solve for  $T$  and  $S$  using linear least-squares regression, Eq. (2.5).



(a)



(b)

**Figure 2.5. Simulation results for determination of the effective temperature. (a) Area fraction of hot spots was varied as indicated and (b) Background hot spot emissivity ratio was varied as indicated.**

The wavelength range used for the simulation results shown in Fig. 2.5,  $0.75 \mu\text{m} \leq \lambda \leq 0.95 \mu\text{m}$ , was the same as that used for the spectrometer measurements. The hot-spot temperature was fixed at  $T_h = 3000 \text{ K}$ . The background temperature was varied,  $500 \text{ K} \leq T_b \leq 3000 \text{ K}$ . Fig. 2.5(a) shows the results for  $\varepsilon_h = \varepsilon_b$  and varying area fraction,  $f_h$ , of hot spots. The effective temperature is the same as the hot-spot temperature if  $T_b = T_h$  or if  $T_b$  is less than about one-third of  $T_h$ . In the intermediate range, the effective temperature depends on the percentage of hot-spot area (hot area). In any case, the effective temperature is always a lower limit for the hot-spot temperature. When compared to a spatial average temperature,  $f_h T_h + (1-f_h)T_b$ , it is clear from Fig. 2.5(a) that the effective temperature is strongly biased toward the hot-spot temperature. This is a consequence of the highly non-linear temperature dependence of blackbody radiation (Fig. 2.3). Similar results were obtained for the simulations shown in Fig. 2.5(b), where the emissivity ratio,  $\varepsilon_b/\varepsilon_h$ , was varied with  $f_h = 0.05$  (5 % hot spots). It should be noted that the form of the curves in Fig. 2.5 is not sensitive to the choice of the temperature  $T_h = 3000 \text{ K}$  used for the simulations. Similar conclusions would be reached if, for example, simulations were run using  $T_h = 1500 \text{ K}$ .

Although we cannot determine the hot-spot area fraction or the background temperature for the experimental tests, the fact that excess m phase remains in the ground surfaces [14] indicates that the overall background temperature must be below the  $m \rightarrow t$  transformation temperature at  $1513 \text{ K}$  (Fig. 2.1). For a reasonable estimate of grinding conditions, say background temperature the order of  $1000 \text{ K}$  and 5 % hot-spot area, Fig. 2.5 shows that the effective temperatures in Table I closely represent the grinding hot-spot temperature,  $T_h$ .

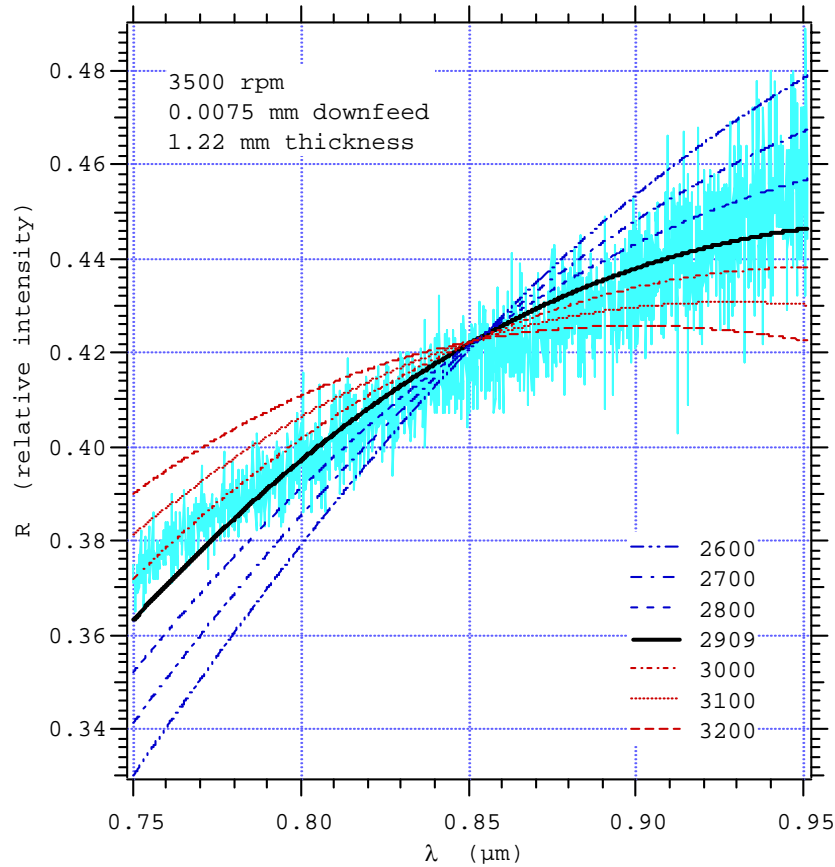


**Figure 2.6. Best-fit blackbody curves for a range of temperatures. The  $R(\lambda)$  vs.  $\lambda$  spectrometer data used is the same as that shown in Fig. 2.4(c).**

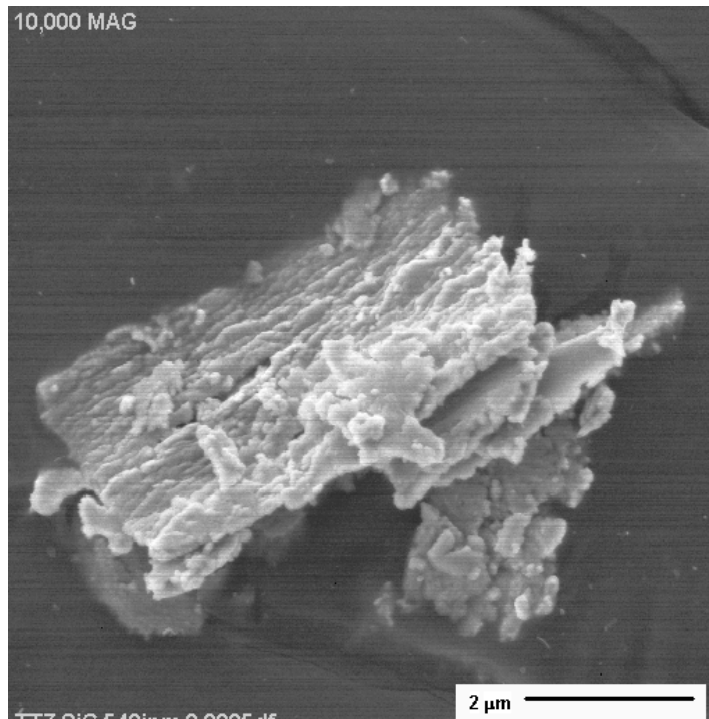
While the reproducibility of the temperature measurements summarized in Table I is quite good in almost all cases, it is pertinent to address the potential variability introduced by “shape matching” measured spectra with blackbody curves. Results for this are shown in Fig. 2.6. The  $R(\lambda)$  curve shown in Fig. 2.4(c) is used for illustration. Best fits to the measured data were obtained using the non-linear regression method discussed in the Appendix. For convenience, the  $R(\lambda)$  data were represented by a second-order polynomial fit (dashed curve in Fig. 2.4(c)). The global best-fit curve is shown as the solid line in Fig. 2.6. The effective temperature obtained, 2909 K, differs from the value of 2923 K obtained in Fig. 2.4(c) using Eq.

(2.5). Numerical differences introduced using the two regression schemes account for this small discrepancy. The remaining curves in Fig. 2.6 show the best-fit blackbody curves for a range of temperatures,  $\pm 300$  K, around 2909 K. These correspond to best-fit deviations larger than the minimum shown in Fig. A1. Based on the visual differences for curve matching seen in Fig. 2.6, and given the scatter in the measured  $R(\lambda)$  data, it is apparent that the curve-matching strategy underlying the spectrometer data analysis method should produce effective temperatures that are reliable within a  $\pm 300$  K uncertainty band.

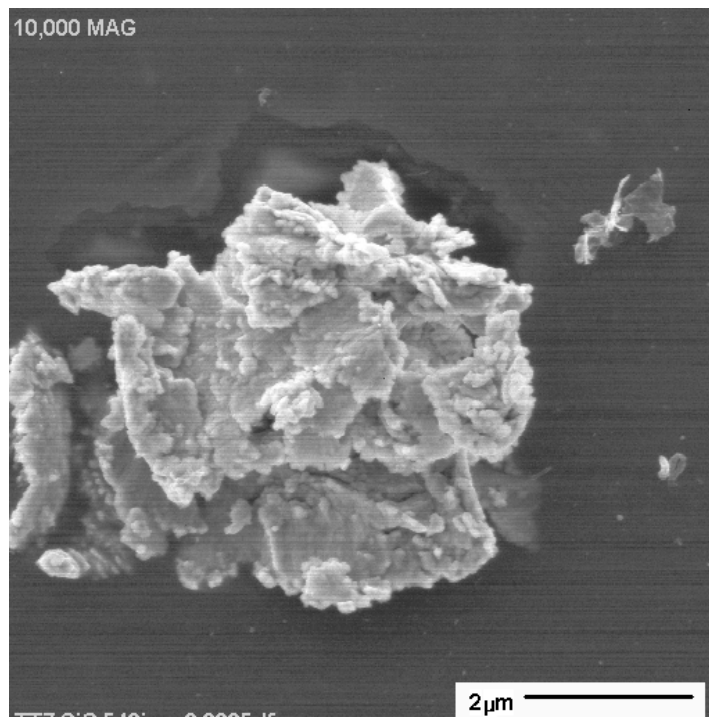
X-ray diffraction measurements made in a companion study [14] showed that the as-received PSZ samples contained approximately 10 % of m phase. After grinding, the surface layer contained 16 - 21 % m phase, depending on the grinding conditions. Excess m phase in the ground-surface layer is the expected response because metastable t phase particles present in the as-received material will transform under the action of the grinding contact stresses [13]. In contrast, the SiC-ground chips did not contain any detectable m phase, and diamond-ground chips contained reduced amounts of m phase on the order of 4 - 5 %. This can be rationalized in terms of the thermomechanical history of the grinding chips. Since grinding chips are detached from the surface after their formation, the thermal response of the chips in a nominally stress-free state dictates their final c + t + m phase content. The detached chips will be very hot, which we can assume to be on the order of the hot-spot temperatures of 3000 K (Table 1). Contact with the grinding coolant will produce rapid quenching of the small chips. Based on the equilibrium phase diagram (Fig. 2.1), the m  $\rightarrow$  t transformation will occur above 1513 K (1240 C) and at even higher temperatures, mixtures of c phase and liquid would be stable. However, it is not expected that the resolution or nucleation and growth transformations would occur because of kinetic constraints imposed by the very high heating/cooling rates. Such constraints would not

affect the  $m \rightarrow t$  martensitic reaction, and it is reasonable to conclude that the phase change occurring in grinding chips above 1513 K is the  $m \rightarrow t$  reversion of the existing  $t$ -phase particles. Then, assuming that the particle size is small enough (subcritical) to suppress the  $M_s$  temperature below room temperature, there would be no  $m$  phase formed in nominally stress-free, detached grinding chips during cooling. This was the case for SiC-ground chips. Some residual  $m$  phase remained in diamond-ground chips, presumably because the high thermal conductivity of diamond modifies the chip-temperature profile. The ground surfaces contain  $m$  phase since they are at temperatures below 1513 K. Their phase content is determined by the stress history, rather than thermal effects. Finally, the occurrence of  $m$  phase in the as-received samples is attributed to processing history and the grinding/polishing operations used to prepare the virgin surfaces.

As noted earlier, the individual amounts of  $c$  and  $t$  phases cannot be detected by x-ray measurements because of overlap of the diffraction peaks. Therefore, x-ray data does not reveal changes in the amount of  $t$  phase in the grinding chips, relative to the as-received material, that might have occurred during their thermomechanical history. Definitive evidence for the proposed scenario based on chip-temperature driven reversion of  $m$  phase in subcritical size  $t$ -phase particles would require TEM investigation of the microstructures present. Notwithstanding the difficulties in preparing TEM specimens from grinding swarf, this kind of study was beyond the scope of the present investigation.



(a)



(b)

**Figure 2.7. SEM micrographs of grinding chips obtained using a SiC grinding wheel. The grinding conditions were: 0.0127 mm downfeed and 2.91 mm<sup>2</sup>/s material removal rate for both (a) and (b).**

In addition to causing the reversion of the m phase, very high temperatures would also facilitate the formation of mechanically soft, ductile grinding chips. Thermal softening effects are considered to be a primary contributing factor for the unique success of properly selected SiC grinding wheels for high material-removal rate, high G-ratio of grinding MgO-PSZ ceramics [16]. Usual experience dictates that hard structural ceramics cannot be ground with common abrasives such as SiC because the high grinding forces must lead to excessive wear and/or damage of the grinding grit. Higher-cost diamond grinding must be used.

SEM observations of the PSZ grinding chips were reported in a companion study [14]. Typical results for SiC-ground chips are shown in Fig. 2.7(a) and 2.7(b), respectively. Ductile-like chip morphology, similar to metal machining, can be found on the chips as is seen in Fig. 2.7(a). Furthermore, the chips often show the granular/globular appearance seen in Fig. 2.7(b). Although not conclusive, the latter is suggestive of partial melting of the chip surface, consistent with very high chip temperatures. Similar features were found for diamond grinding wheels, and in this case long ductile-like chips were present. Presumably this is due to the sharper cutting edges presented by diamond grit compared to SiC grit. Even with the high hot-spot temperatures, diamond grit is a robust grinding media for PSZ, suggesting that the high thermal conductivity of diamond must prevent the grits from experiencing excessive thermal degradation.

## 2.6. Summary and Conclusions

A spectrometer method was developed to measure the grit-workpiece interface temperatures for grinding 9 mol % MgO-PSZ. Advantage was taken of the fact that PSZ is semi-transparent in the near infrared and measurements were made using transmitted light. Effective temperatures on the order of 3000 K were obtained for the grinding conditions used. Simulations



were made which showed that the effective temperatures measured are representative of the peak hot-spot temperatures reached during grinding. This is consistent with high grinding chip temperatures, which result from the very low thermal conductivity of PSZ. The high chip temperature causes reversion of the monoclinic phase to tetragonal phase in the grinding chips, whereas the ground surfaces contain excess monoclinic phase. Very high chip temperatures can also produce ductile-like grinding response. This effect appears to underlie the success for SiC-grinding of PSZ components in high-volume production applications.

## References

- [1] S. Malkin and R. B. Anderson, 1974, "Thermal Aspects of Grinding, Part 1: Energy Partition," *Jour. Eng Ind*, Vol. 96, pp. 1177-1183.
- [2] H. L. Costa, V. C. Pandolfelli, and J. D. Biasoli de Mello, 1997, "On the Abrasive Wear of Zirconias," *Wear* 203-204, pp. 626-636.
- [3] M. V. Swain and R. H. J. Hannink, 1989, "Metastability of the Martensitic Transformation in a 12 mol% ceria-zirconia alloy: II, Grinding Studies," *J. Am. Ceram. Soc.*, Vol. 72, No. 8, pp. 1358-1364.
- [4] T. Ueda, K. Yamada, and T. Sugita, 1992, "Measurement of Grinding Temperature of Ceramics Using Infrared Radiation Pyrometer with Optical Fiber" *Jour. Eng Ind.*, Vol. 114, pp. 317-321.
- [5] B. Zhu, C. Guo, J. E. Sutherland and S. Malkin, 1995, "Energy Partition to the Workpiece for Grinding of Ceramics." *Annals Intl Inst. Prod. Engr. Res., Man Tech*, Enschede, Netherlands, pp. 21-26.
- [6] S. Kohli, C. Guo, and S. Malkin, 1995, "Energy Partition to the Workpiece for Grinding with Aluminum Oxide and CBN abrasive wheels," *Jour. Eng Ind.*, Vol. 117, pp. 160-168.
- [7] R. R. Hebbbar, S. Chandrasekar, and T. N. Farris, 1992, "Ceramic Grinding Temperatures," *J. Am. Ceram. Soc.*, Vol. 75, No. 10, pp. 2742-2748.

- [8] S. Chandrasekar, T. Farris, and B. Bhushan, 1990, "Grinding Temperatures for Magnetic Ceramics and Steel," *Jour. Trib.*, Vol. 112, pp. 535-541.
- [9] T. N. Farris and S. Chandrasekar, 1990, "High-Speed Sliding Indentation of Ceramics: Thermal Effects," *Jour. Mat. Sci.*, Vol. 25, pp. 4047-4053.
- [10] T. Ueda, A. Hosokawa, and A. Yamamoto, 1985, "Studies on Temperature of Abrasive Grits in Grinding-Application of Infrared Radiation Pyrometer," *Jour. Eng Ind.* Vol. 107, pp. 127-133.
- [11] J. O. Outwater and M. C. Shaw, 1952, "Surface Temperatures in Grinding" *Trans ASME*, pp. 73-86.
- [12] J. A. Griffioen, S. Bair and W. O. Winer, 1985, "Global Studies of Mechanisms and Local Analyses of Surface Distress Phenomona," Inst. National des Sciences Appliquees, Lyon France, pp. 3-6 Sept.
- [13] R. Stevens, 1986, *Zirconia and Zirconia Ceramics*, Magnesium Elektron Publication No. 113, Magnesium Elektron Ltd., Manchester, U.K.
- [14] A. J. Shih, R. O. Scattergood, A. C. Curry, T. M. Yonushonis, D. J. Gust, M. B. Grant, S. B. McSpadden, 2003, "Grinding of Zirconia using the Dense Vitreous Bond Silicon Carbide Wheel," *Jour. Manuf. Sci. and Engr.*, Vol. 125, pp. 297-303.
- [15] A. C. Curry, 2001, *Methods of Measuring Flash Temperatures in the Grinding of MgO-PSZ*, MS Thesis, North Carolina State University.
- [16] A. J. Shih and T.M. Yonushonis, 2000, *High Infeed Rate Method for Grinding Ceramic Workpiece with Silicon Carbide Grinding Wheels*, US Patent Number 6,030,277.
- [17] D. Ng and G. Fralick, 1999, "Temperature Measurement of Ceramic Materials Using a Multi-wavelength Pyrometer," NASA Lewis Research Center, NASA TM 1999-208850.
- [18] D. Ng, 1997, "Temperature Measurement of a Glass Material Using a Multi-wavelength Pyrometer," NASA Lewis Research Center, NASA TM 1997-107433.
- [19] C. F. Grain, 1967, "Phase Relations in the  $ZrO_2$ -MgO System", *J. Am. Ceram. Soc.*, Vol. 50, No. 6, pp. 288-290.

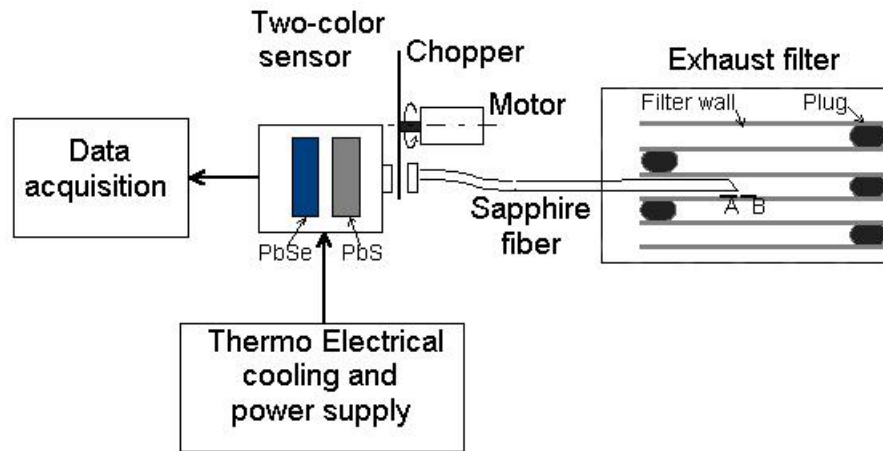
## **CHAPTER 3. INFRARED THERMOMETRY FOR DIESEL EXHAUST AFTERTREATMENT FILTER TEMPERATURE MEASUREMENT**

### **3.1. Introduction**

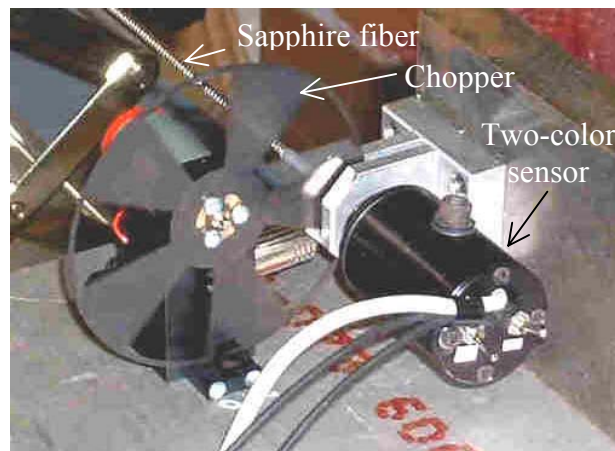
Worldwide environmental regulations have established stringent targets for future clean diesel engines and have driven the development of exhaust aftertreatment technologies to remove environmentally harmful nitrogen oxide (NO<sub>x</sub>) and particulate matter (PM) from diesel exhaust. To meet the low emission requirements, filters are used to capture diesel NO<sub>x</sub> and PM emissions. Periodically, the regeneration process is activated to elevate the filter temperature to initiate chemical reactions of stored NO<sub>x</sub> and PM. Several heating methods, such as the post injection of fuel [1] and microwave heating [2], have been developed for filter regeneration.

Diesel exhaust aftertreatment filters are typically made of porous ceramic material with deep cavities or channels to increase the specific surface area. Attaching thermocouples to the porous ceramic wall surface at locations deep within the filter cavity is difficult due to the space constraints. The harsh environment in the filter, which is subject to high temperature engine combustion airflow as well as thermal cycling as a consequence of periodical regeneration, also makes the connection of thermocouple tip to filter wall surface technically challenging. Thermocouples inserted inside the cavity measure the air, not the filter surface, temperature. If the microwave heating method is used, the application of traditional thermocouples is prohibited due to their inherently metallic composition. As an

alternative to using a thermocouple, an optical fiber can be employed to transmit the emitted surface thermal radiation to an infrared detector for temperature measurement, as illustrated in Fig. 3.1.



(a)



(b)

**Figure. 3.1.** The application of PbS-PbSe two-color sensor and sapphire optical fiber for measurement of diesel exhaust aftertreatment filter temperature; (a) experiment setup (b) close-up view of the two-color sensor, chopper, and sapphire fiber.

The temperature on filter surfaces controls the chemical kinetics of the storage and regeneration of NO<sub>x</sub> and PM. The accurate, in-situ measurement of filter surface temperature is important for the development of new diesel exhaust aftertreatment techniques. New catalytic technologies have been applied to lower the regeneration temperature, which is beneficial for engine fuel efficiency. To study the effectiveness of new catalysts and its effects on the storage and regeneration process, accurate filter wall temperature data is required. A uniform temperature distribution in the filter is important in controlling the homogeneous chemical reactions as well as avoiding thermal stress fatigue and overheating the filter. Precise thermal mapping of the filter was achieved by measuring the surface temperature at various locations within the filter. Using an optical fiber with 45° angled tip, the field of view of the fiber tip can be narrowed to a small and specific region on the filter wall surface. This was validated in a study to investigate the goniometric characteristic of various shapes of optical fiber tips [3].

The diesel engine exhaust temperature, depending on the operating conditions, ranges from 100 to 550°C [1,4–7]. A temperature range from 250 to 500°C is required for good NO<sub>x</sub> conversion efficiencies [8,9] and a lower temperature limit between 250 to 350°C is required for particulate regeneration [4]. The advancement in catalyzed technology has further reduced the regeneration temperature for NO<sub>x</sub> and particulate filters. For infrared thermometry, low temperatures do not generate strong thermal emissive power. This is one of the technical challenges in this study. In order to cover a wide range of engine operations and filter storage and regeneration conditions, as well as map the temperature profile in the filter, a measurement method capable to cover a wide range of temperature is particularly important. The two goals of this study are to develop an optical fiber and infrared sensor

based temperature measurement system for diesel exhaust aftertreatment filters and to explore the limit of this system to measure low temperatures below 150°C.

Components and features of the system, which include the optical fiber, goniometric characteristics of the fiber tip, and infrared sensor, are first introduced. The temperature measurement strategy using the one-color and two-color methods and sensor calibration are then presented. Results of the temperature measurement experiments conducted in a microwave heated filter are analyzed and compared.

## **3.2. Infrared-based Temperature Measurement System**

The configuration of the infrared temperature measurement system is shown in Fig. 3.1(a). A single crystal sapphire fiber with 45° angled tip was inserted into a cavity in exhaust aftertreatment filter to collect infrared radiation emitted from the filter wall surface. The system consists of the optical fiber and sensor, which are discussed in the following two sections.

### **3.2.1 Single Crystal Sapphire Fiber**

Single crystal sapphire ( $\text{Al}_2\text{O}_3$ ) is selected as the optical fiber material. Sapphire is transparent from the visible to approximately 4.5  $\mu\text{m}$  wavelength [10]. Based on transmission tests conducted by Photran LLC, sapphire fiber has high transmission from the visible to beyond 3.5  $\mu\text{m}$  spectrum, making it suitable to transmit far infrared radiation in the 100 to 600°C ranges from the filter wall surface to the infrared detector. Sapphire is also transparent to microwave radiation, which allows its use for the in-situ, non-contact

temperature measurements during the microwave heating for filter regeneration. Other unique properties of sapphire include a high melting temperature, high elastic modulus to reduce the fiber bending, and good chemical and erosion resistance. These properties make the single crystal sapphire ideal for the diesel exhaust filter temperature measurement. A single crystal sapphire fiber, manufactured by Photran LLC, was used in this study. This fiber is 1 m long and 0.425 mm in diameter.

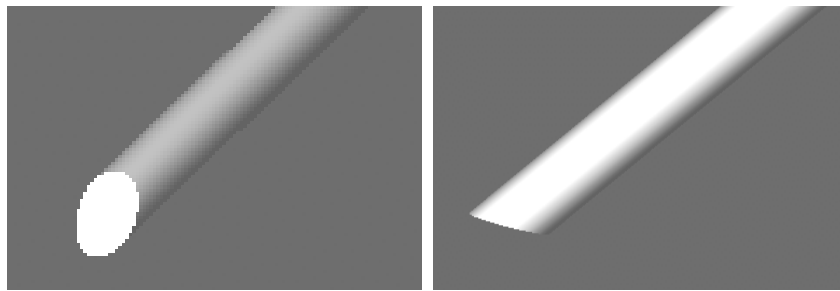


**Figure 3.2. Sapphire fiber with 45° angled tip.**

The sapphire fiber has a polished 45° angled tip, as shown in Fig. 3.2. Boothe et al. [3] have studied the goniometric characteristics of this fiber tip geometry and proven that the 45° angled tip fiber gathers thermal radiation from a small and specific region perpendicular to the fiber axis. The setup of experiment using the angular scan method to determine the field of view of an optical fiber with 45° angled tip is shown in Fig. 3.3. A light source rotated around the fiber tip and a Lead Sulfide (PbS) and Lead Selenide (PbSe) two-color infrared sensor was used at the other end of the fiber to detect the intensity of light emission transmitted through the fiber. The relative angle between the fiber and light source is designated as  $\alpha$ . At  $\alpha = -90^\circ$ , the light source was aiming at the polished face of the fiber; at  $\alpha = 0^\circ$ , the light source was along the fiber axis; at  $\alpha = 90^\circ$ , the light source was located

opposite to the polished face of the fiber tip. The light source reached position limit at  $\alpha = 140^\circ$ . Results of relative intensity of light received by the infrared sensor vs.  $\alpha$  are shown in Fig. 3.3. The major peak appears at  $\alpha = 90^\circ$ . This is due to the reflection of the thermal radiation off the polished face inside the fiber, as shown by the arrow sign in Fig. 3.3. A small hump, about only 9% of the relative intensity of the peak, can be seen at  $\alpha = 18^\circ$ . As shown in Fig. 3.1(a), when the  $45^\circ$  angled tip fiber was used inside a cavity in the diesel filter, the fiber tip collected most of the thermal radiation from the filter wall surface at A, which corresponds to the  $\alpha = 90^\circ$  peak in Fig. 3.3. A small portion of thermal radiation at B in front of the fiber tip was also transmitted to the infrared sensor due to the hump in Fig. 3.3.

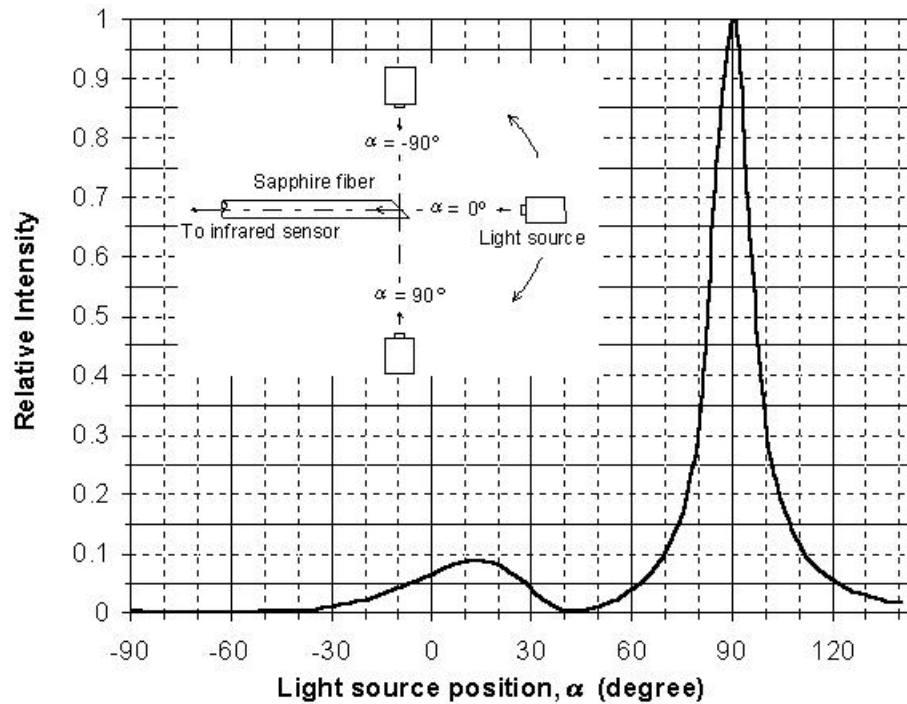


**Figure 3.3. Goniometric characteristics of 45° angled tip sapphire optical fiber [3].**



### 3.2.2. PbS/PbSe Two-Color Infrared Sensor

According to the Wien's displacement law [11], in the 150 to 400°C temperature range for aforementioned diesel exhaust gas and filter regeneration, blackbody radiation peaks between wavelengths at 4.3 to 6.8  $\mu\text{m}$ . The PbS and PbSe infrared sensor, which have peak intensity at 2.5 and 3.7  $\mu\text{m}$ , respectively, are selected to achieve good sensitivity of the two-color infrared detector. Both the PbS and PbSe are photoconductors sensitive only to an AC signal [12]. A mechanical chopper was used in front of the sensor's connection to the optical fiber to generate an AC light signal input. In this study, the chopping frequency was 250 Hz. The sensor was cooled by a BiTe thermal-electric cooler (TEC) to  $-30^\circ\text{C}$  to enhance its sensitivity and stability. A picture of the setup, including the sensor, chopper, and sapphire fiber, is shown in Fig. 3.1(b). The PbS/PbSe two-color sensor has a sandwiched construction. Only one infrared input is required for the sensor. This has eliminated the needs to split the light to two infrared detectors. As illustrated in Fig. 3.1(a), the PbS detector is placed in front of the PbSe detector to receive the thermal radiation from the optical fiber.

The PbS and PbSe detectors converted the radiation into two different AC voltage outputs. The output AC signals were then recorded by a PC data acquisition system, which utilizes the LabView program for data analysis. The root-mean-square (RMS) value of the output AC signal was calculated to represent the detector output for calibration and temperature measurement.

The PbS and PbSe used in this study are two wide-band infrared detectors. The narrow band infrared detectors using spectrally selective filters were not considered in this

study because it limits the intensity of light received and the low temperature measurement capability. As reported by Wickersheim [13], the low temperature that can be detected by the narrow band infrared detector is limited to about 300°C. The relative intensity of the PbS and PbSe detector vs. wavelength, the data provided by the sensor manufacturer (Electro-Optical Systems Inc.), is shown in Fig. 3.4. The PbS and PbSe detectors are sensitive to infrared radiation from 1.0 to 2.8  $\mu\text{m}$  and from 2.8 to 4.5  $\mu\text{m}$  wavelength, with peaks at 2.5 and 3.7  $\mu\text{m}$ , respectively. Both PbS and PbSe detectors have about 1.8  $\mu\text{m}$  broad spectrumrange of detection and are considered as wide-band two-color sensor.

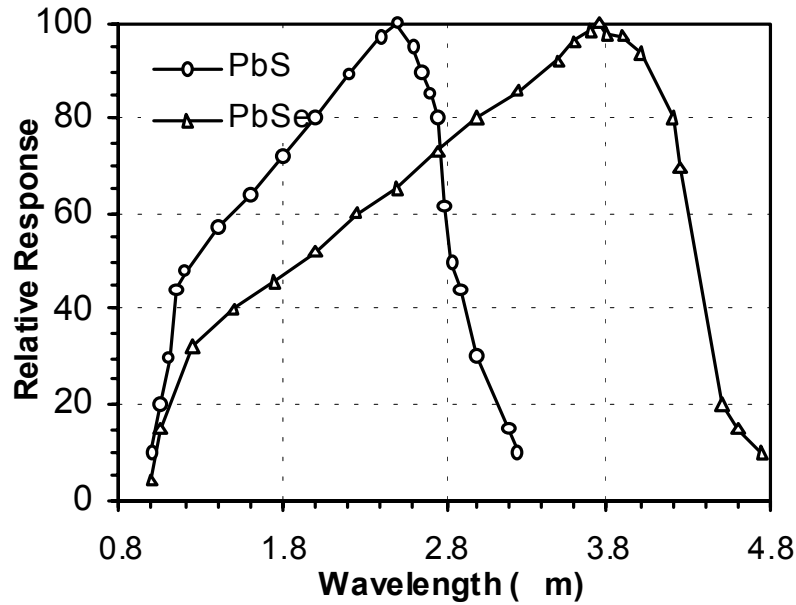


**Figure 3.4. The relative intensity of the detectors vs. wavelength.**

By viewing a blackbody radiation source through the single crystal sapphire fiber, the voltage vs. temperature outputs of the PbS and PbSe detectors were measured and results are shown in Fig. 3.5. The voltage output from PbSe, which is placed behind PbS, is generally weaker than that of PbS. The PbSe has a peak at a higher wavelength and, in theory, should

be more sensitive to thermal radiation response at low temperature. At 400°C, the blackbody spectrum radiation peaks at  $\lambda = 4.3 \mu\text{m}$ . For temperatures lower than 400°C, the PbSe detector, which has peak response at 3.7  $\mu\text{m}$  vs. 2.5  $\mu\text{m}$  of PbS (Fig. 3.4), can receive more thermal radiation power than the PbS detector. However, the PbS detector in a sandwich construction blocks the thermal radiation signal received by the PbSe detector. The cut off of radiation signal beyond 3.5  $\mu\text{m}$  for the single crystal sapphire fiber is another possible cause for the low voltage output of PbSe. Voltage outputs from two detectors were applied to calculate the temperature.

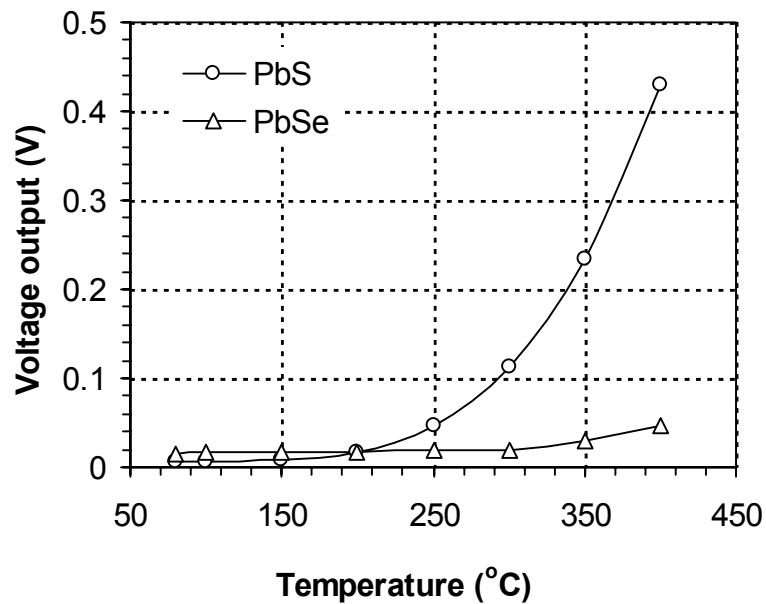


Figure 3.5. PbS and PbSe detector voltage output vs. temperature.

### 3.3. Temperature Measurement and System Calibration

#### 3.3.1. Radiation Thermometry Methods

Infrared radiation thermometry measures the absolute intensity of radiation emanating from a target surface. A calibration method is established to convert the measured radiation signal in DC voltage to temperature. The relationship between the radiance and temperature of a blackbody is described by the Planck's law.

$$L_{\lambda,b}(\lambda, T) = \frac{c_{1L}}{\lambda^5 (e^{\frac{c_2}{\lambda T}} - 1)} \quad (3.1)$$

where  $c_{1L} = 1.191 \times 10^8 \text{ W} \cdot \mu\text{m}^4 \cdot \text{m}^{-2} \cdot \text{sr}^{-1}$  and  $c_2 = 1.439 \times 10^4 \text{ } \mu\text{m} \cdot \text{K}$  are the first and second radiation constants and  $T$  is the absolute temperature. The single-wavelength or one-color thermometry method infers the target surface temperature by measuring the radiance in a selected infrared spectrum. The voltage output from the detector  $V(\lambda)$  at a specific wavelength  $\lambda$  is

$$V(\lambda) = \varepsilon(\lambda)\tau(\lambda)R(\lambda)L_{\lambda,b}(\lambda, T) \quad (3.2)$$

where  $\varepsilon(\lambda)$  is the emissivity of the emitting surface,  $\tau(\lambda)$  is the transmissivity of the optical fiber and intervening media, and  $R(\lambda)$  is the gain of detector, which is the spectral electrical response constant at wavelength  $\lambda$ . For the wide-band detector (Fig. 3.4) used in this study, the radiance received by the detector, represented by the voltage output  $V$ , can be expressed as an integral across the range of wavelength, from  $\lambda_L$  to  $\lambda_H$ , sensitive to the detector.

$$V = \int_{\lambda_L}^{\lambda_H} \varepsilon(\lambda) \tau(\lambda) R(\lambda) L_{\lambda,b}(\lambda, T) d\lambda \quad (3.3)$$

The target surface emissivity  $\varepsilon(\lambda)$  and fiber and media transmissivity  $\tau(\lambda)$  are generally not known in most practical applications. Calibration is needed to determine the temperature  $T$  using the one-color thermometry method.

The two-color thermometry method measures the infrared radiance at two wavelength regions. The voltage ratio from the two wavelength outputs is used to evaluate the target temperature. The two PbS and PbSe wide-band infrared detectors used in this study, marked by 1 and 2, are sensitive in the wavelength region from  $\lambda_{1L}$  to  $\lambda_{1H}$  and  $\lambda_{2L}$  to  $\lambda_{2H}$  and have voltage output  $V_1$  and  $V_2$ , respectively. Two-color thermometry method assumes that  $\varepsilon(\lambda)$  and  $\tau(\lambda)$  remain constant from  $\lambda_{1L}$  to  $\lambda_{1H}$  and from  $\lambda_{2L}$  to  $\lambda_{2H}$ . With this assumption, the ratio  $V_1/V_2$  can be expressed as:

$$\frac{V_1}{V_2} = \frac{\int_{\lambda_{1L}}^{\lambda_{1H}} R(\lambda) L_{\lambda,b}(\lambda, T) d\lambda}{\int_{\lambda_{2L}}^{\lambda_{2H}} R(\lambda) L_{\lambda,b}(\lambda, T) d\lambda} \quad (3.4)$$

Practically, emissivity and transmissivity change with respect to wavelength. By choosing the two wavelength regions as close as possible, the error can be minimized.

### 3.3.2. Temperature Measurement Strategy

As shown in Fig. 3.1(a), the diesel exhaust aftertreatment filters have deep channels to increase the specific surface area. The length to width ratio of a channel is typically over

30. The porous ceramic filter wall surface is a good diffuse emitter. Both of these characteristics make it suitable to approximate the filter cavity as a blackbody. With this simplification, one-color thermometry method can be used for temperature measurement.

The one-color method is based on the thermal radiation intensity received by the detector. This intensity may change due to the different levels of soot and NO<sub>x</sub> loading on the filter surface. The variation in airflow rate and the soot density can also change the transmissibility during temperature measurement across a wide range of filter operation conditions. The two-color thermometry method is less sensitive to the changing of environmental conditions and can provide better accuracy for temperature measurement.

This study used the two wide-band PbS and PbSe infrared detectors for temperature measurement. The one-color thermometry method was used on the PbS detector voltage output for temperature measurement. Using the ratio of the voltage outputs from two detectors, the two-color thermometry method was developed. Results using these two radiation thermometry methods are presented and compared in Sec. 3.4.

### **3.4. Calibration**

As shown in Fig. 3.6, the optical fiber temperature measurement system was calibrated using a blackbody heat source. The blackbody cavity is made of an oxidized Inconel tube. The intrinsic emissivity of the oxidized Inconel wall is about 0.828, which generates a cavity emissivity of 0.997 [14]. The integrating effect of the cavity can minimize the error associated with the estimation of the wall surface emissivity [15]. The blackbody cavity is heated in three zones by resistance heating wires independently controlled by three

PID controllers. Three type K thermocouples are used in three zones shown in Fig. 3.6 to provide temperature feedback and achieve a uniform temperature distribution across the cavity. The calibration test was conducted from 80 to 400°C, the temperature range of particular interest for catalyzed diesel exhaust filters.

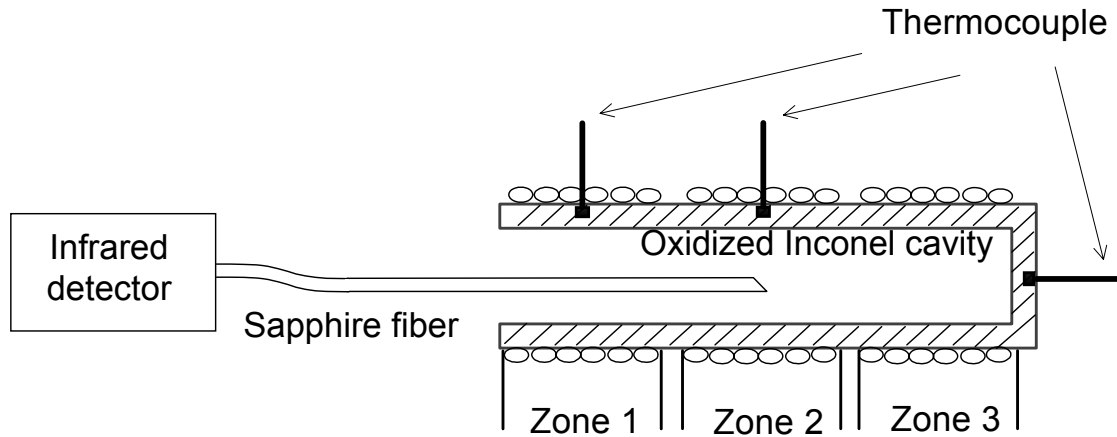


**Figure 3.6. Oxidized Inconel cavity as the blackbody for infrared sensor calibration.**

The voltage signal of the PbS detector, denoted as  $V_{PbS}$ , is used as the one-color thermometer output. As shown in Fig. 3.5,  $V_{PbS}$  is much higher and more distinguishable than the voltage output of the PbSe detector,  $V_{PbSe}$ , for accurate temperature measurement. Fig. 3.7(a) shows the data points acquired from blackbody calibration. Two polynomial calibration curves were used to fit the data points in the 80 to 150°C and 150 to 400°C regions. These two polynomial calibration curves, as shown in Fig. 3.7(a), match well to the data points and can be expressed as:

$$T = 2.18 [\ln(V_{PbS})]^3 - 21.5 [\ln(V_{PbS})]^2 + 123 [\ln(V_{PbS})] + 490 \quad (150^\circ\text{C} < T < 400^\circ\text{C})$$

$$T = 218 \ln(V_{PbS}) + 1201 \quad (80^\circ\text{C} < T < 150^\circ\text{C}) \quad (3.5)$$

For the two-color method, the ratio of  $R = \ln(V_{PbS}/V_{PbSe})$  is used. Fig. 3.7(b) shows the calibration data points of blackbody temperature vs.  $R$ . Similar to Fig. 3.7(a), two calibration curves were used to fit the data points.

$$T = 7.89 R^6 - 25.4 R^5 + 16.0 R^4 + 18.1 R^3 - 17.9 R^2 + 57.7 R + 199 \quad (150^\circ\text{C} < T < 400^\circ\text{C})$$

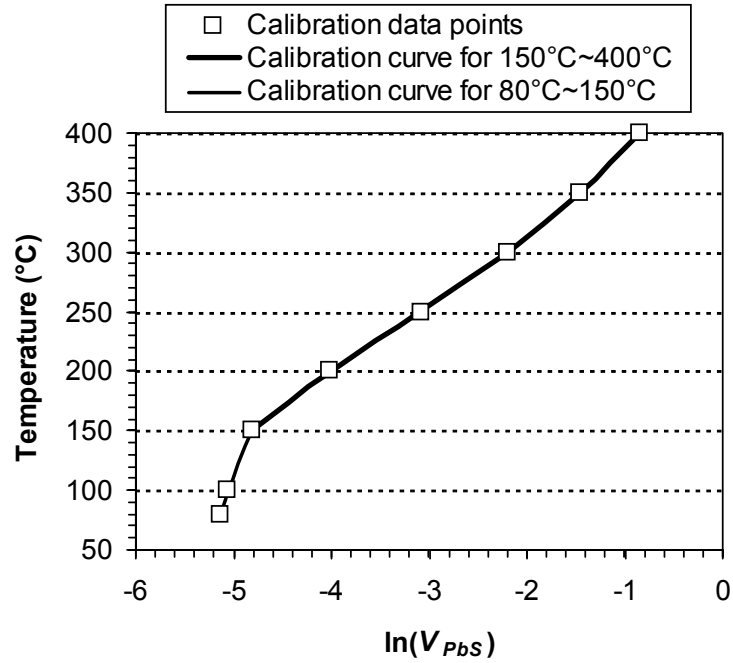
$$T = 278 R + 366 \quad (80^\circ\text{C} < T < 150^\circ\text{C}) \quad (6)$$

Below  $150^\circ\text{C}$ , the temperature is very sensitive to the voltage output. For example, using the two-color calibration curve in Fig. 3.7(b), only when the ratio  $R$  is between a narrow range between  $-0.99$  and  $-0.78$ , the temperature can be predicted. The temperature is also very sensitive to  $R$ . It is concluded that this system has limited accuracy to measure low temperatures between  $80^\circ\text{C} < T < 150^\circ\text{C}$ .

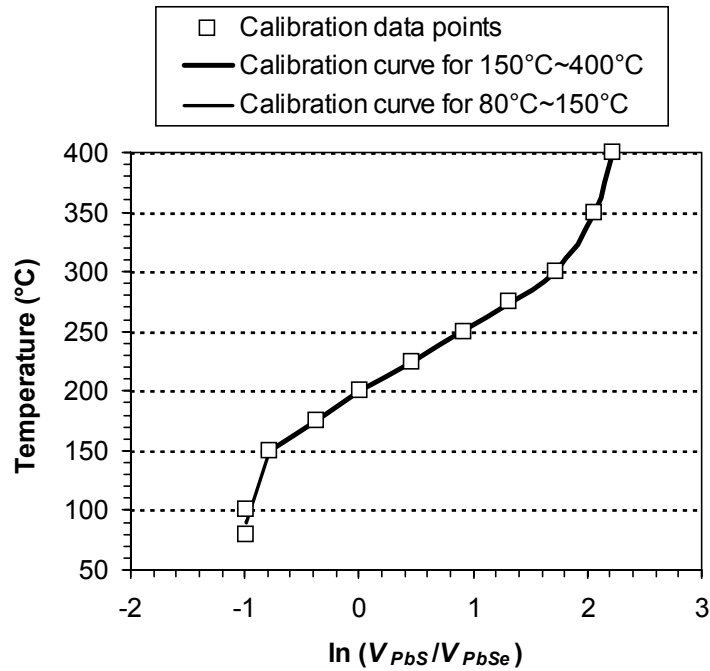
### 3.5. Filter Heating and Temperature Measurement Experiment Setup

A segment of ceramic filter, manufactured by Industrial Ceramic Solutions LLC, was used in the temperature measurement experiment. The filter material, designed to capture airborne fine particulate less than  $10 \mu\text{m}$  in size, consists of long,  $\mu\text{m}$ -level diameter  $\text{Al}_2\text{O}_3$  fiber. Mixed in the  $\text{Al}_2\text{O}_3$  fiber structure are SiC whiskers, which can react quickly and efficiently to convert microwave energy to thermal energy, generating heat in the filter wall and burning the captured diesel particulate during regeneration [16]. Microwave heating is not uniform across the whole filter surfaces, causing hot and cold spots to exist in the filter.





(a)



(b)

**Figure 3.7. Blackbody calibration results; (a) one-color calibration data points and curves and, (b) two-color calibration data points and curves.**

Fig. 3.8 shows the setup for microwave heating of the ceramic filter and temperature measurement. The overall setup with the microwave heater, optical fiber, chopper and chopper control, two-color sensor, TEC control and power supply for sensor, and data acquisition system are shown in Fig. 3.8(a). An array of small holes was drilled through the sidewall of the microwave heater as shown in Fig. 3.8(b). The hole pattern matches to the cavity positions in the filter to assist locating the optical fiber into a specific cavity within the filter. The diameter of the hole is about 3 mm, which is small enough to prevent microwave leakage.

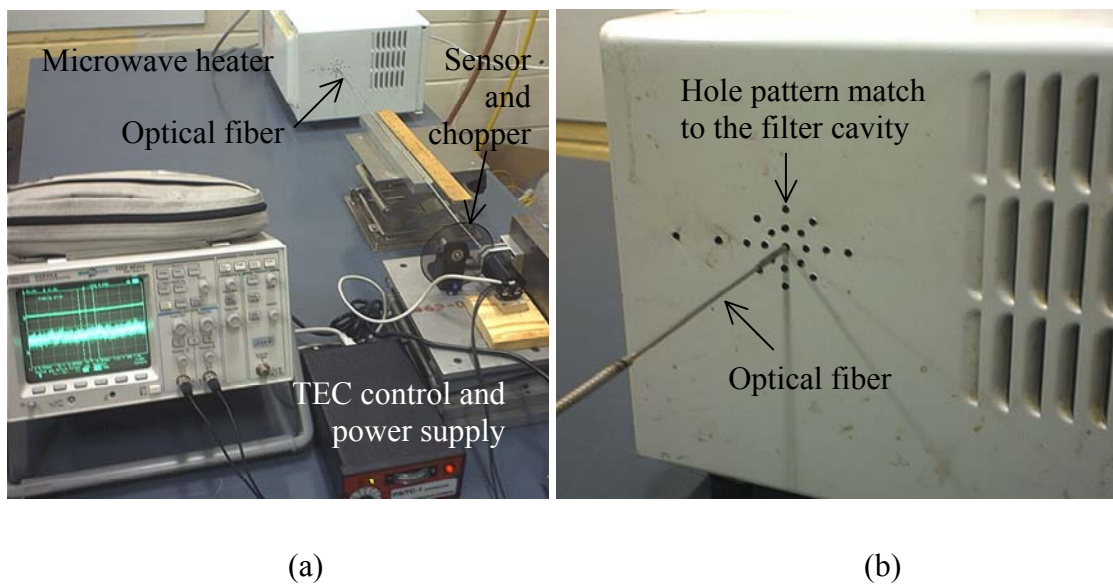


**Figure 3.8. Setup for microwave heating temperature measurement; (a) overview of the sensor, optical fiber, microwave heater, and data acquisition and (b) entry and positioning holes for optical fiber.**

Fig. 3.9 illustrates the side view and front view of the ceramic filter as well as the four locations of the fiber tip used for temperature measurement. The outer diameter of the filter is 55 mm and the length is about 76 mm. The optical fiber tip was placed inside two

cavities, marked by I and II in Fig. 3.9(a). Cavity I is a small hole between the center and side of the filter. Cavity II is the larger hole in the center of the filter. In each cavity, two positions in the center and side of the cavity, marked as “C” and “S”, denote the fiber tip locations. The location “S” is 12 mm from the open end of the filter and the distance between “C” and “S” is 25 mm. Temperature vs. time data at four locations, designated as IC, IS, IIC, and IIS, were recorded.

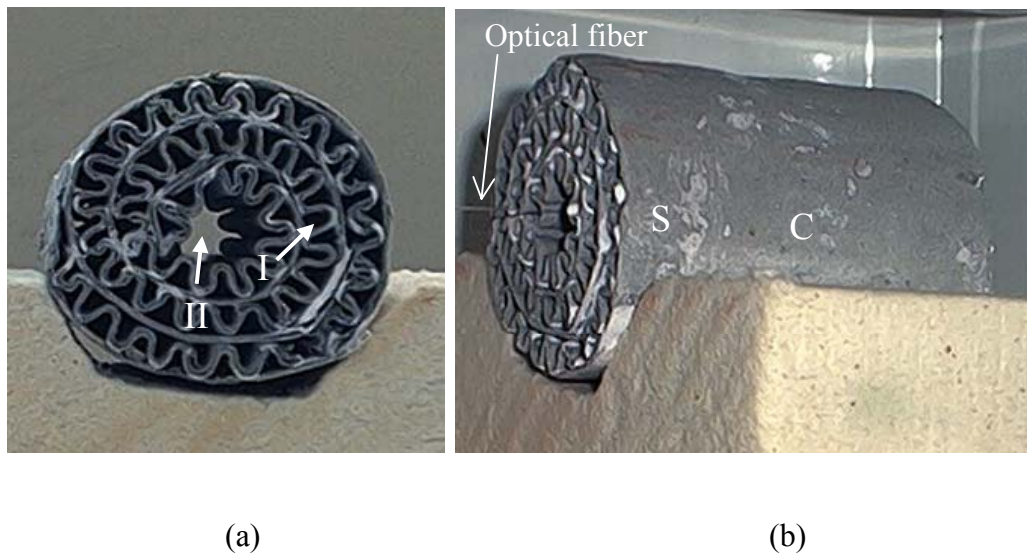


**Figure 3.9. Setup for filter and optical fiber inside the microwave heater; (a) front view of the filter and the designation of cavity I and II and (b) side view of filter with the center, C, and side, S, locations of fiber tip.**

To demonstrate the repeatability of microwave heating at every selected fiber tip location, four repeated temperature measurement tests under the same microwave heating conditions and the same location and orientation of the fiber tip were conducted. In total, 16 sets of temperature vs. time data at four fiber tip positions were collected and analyzed. After each heating test, the filter was cooled to room temperature within the microwave

heater before starting the next heating test. Maintaining the filter's exact location in the microwave oven ensures the same heating process and temperature distribution for each test.

Each microwave heating test lasted for 240 s under a 950 W power setting. The AC voltage outputs of both PbS and PbSe detectors were recorded at 4000 samples per second sampling rate. The RMS value of every 800 data samples was calculated to represent the sensor voltage output every 0.2 s. The RMS voltage was substituted into the calibration curves in Eqs. (3.5) and (3.6) to determine the filter wall temperature.

### 3.6. Temperature Measurement Results and Discussion

Since the sapphire fiber is transparent to microwaves, during temperature measurement, the fiber is not heated by the electromagnetic field and, the electromagnetic field distribution is also not affected by changing the fiber tip location. Experimental results show good repeatability of the microwave heating and temperature measurement. An example is shown in Fig. 3.10. At fiber tip location IIS, the temperature curves of four repeated heating tests and the average of these four tests show the repeatability of the microwave heating process and temperature measurement. The maximum deviation among the four tests is less than 20°C and 10°C for the one- and two-color method, respectively. Fig. 3.11 shows the average measured temperature vs. time results at four fiber tip locations: IC, IS, IIC, and IIS. Heating across the filter is not uniform. Among the four fiber tip locations, the highest heating rate was observed at IC, i.e., inside cavity I. The temperature steadily increased to 400°C in 60 s. In comparison to fiber tip location IIC (inside cavity II), it took about 90 s to reach 400°C. Close to the side of the filter at fiber tip locations IS and IIS, the heating rate was about the same; both took about 120 to 140 s to reach 400°C. Due

to the non-uniform electromagnetic field intensity in microwave heating, the filter center region had a higher heating rate than on the side of the filter. The discrepancy in heating rate across the filter surface generates the non-uniform temperature distribution and chemical reaction for regeneration. The temperature gradient in the filter also creates thermal stresses and thermal cycle fatigue problem.

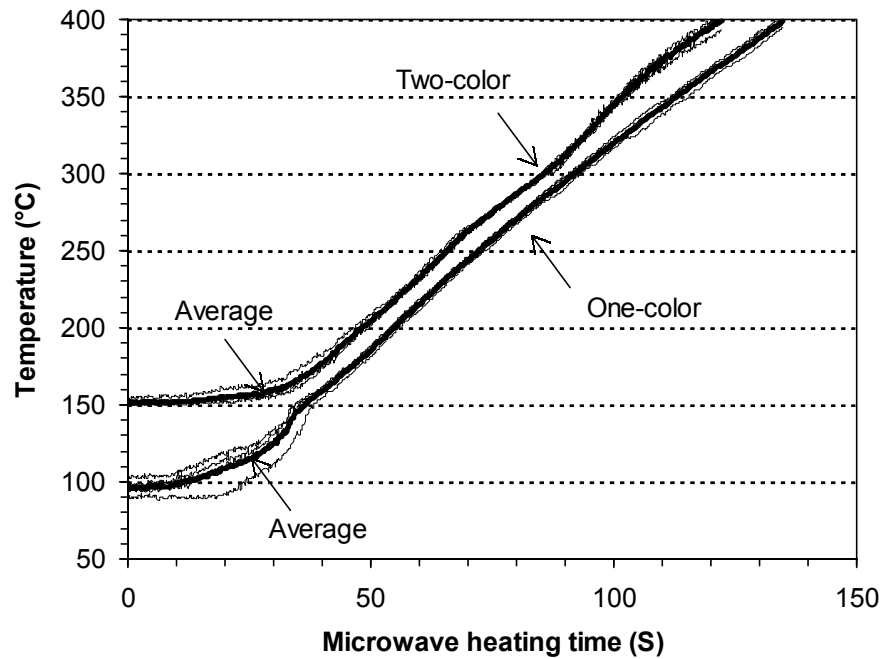


**Figure 3.10. Temperature repeatability at location IIS.**

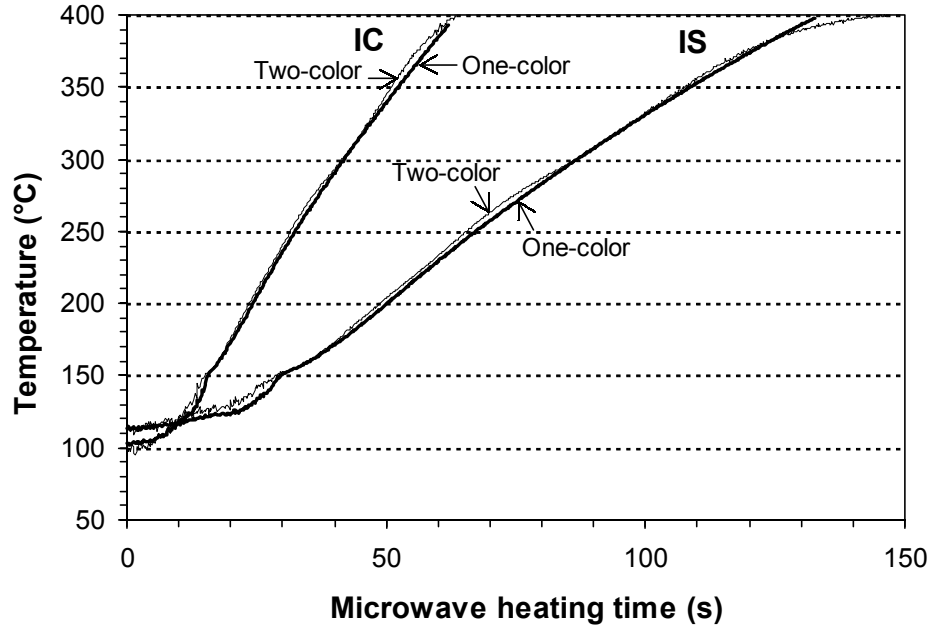
At the two fiber tip locations in Cavity I, as shown in Fig. 3.11(a), results of temperature measured using the one-color and two-color method closely match each other between 150 to 400°C. Such good agreement does not repeat at the two fiber tip locations in Cavity II. The two-color method generally predicts higher temperature than the one-color method. As shown in Fig. 3.11(b), the discrepancy is about 20 to 30°C. Cavity I, as shown

in Fig. 3.9, has much smaller cross-sectional area and larger aspect ratio than Cavity II, which is the large size hole in the center of the filter. Due to the multi-reflection emissivity enhancement effect in the cavity with large aspect ratio, Cavity I has close to 1.0 effective emissivity and is almost a blackbody. This result is seen in the good match of the one- and two-color temperature measurement methods in Cavity I (Fig. 3.11(b)).

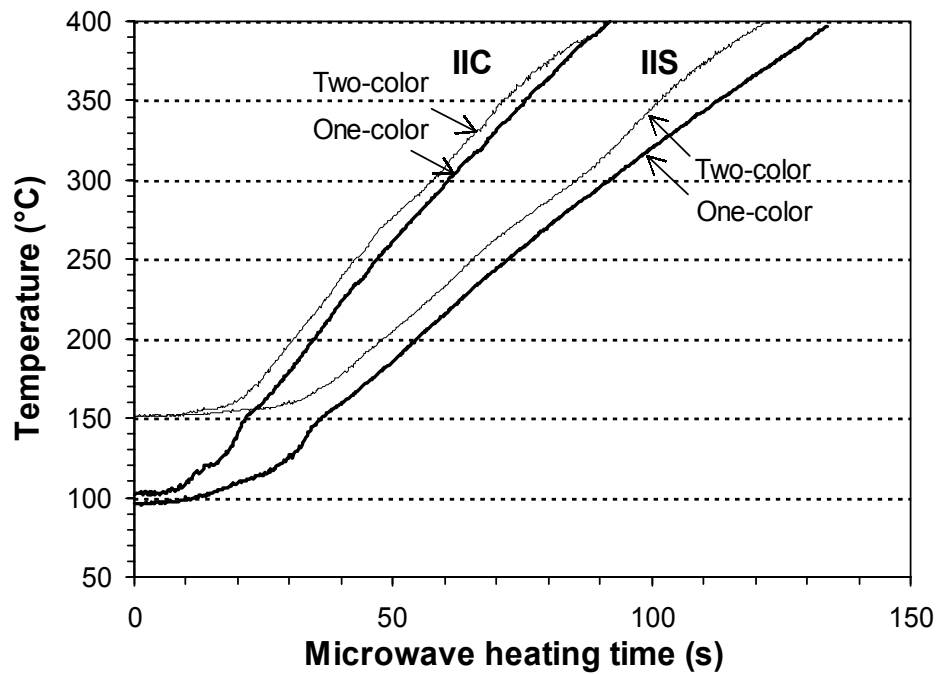
The temperature calculated by the two-color method is generally higher than that predicted using the one-color method. This can be explained by the difference in temperature measurement strategy. The one-color method relies on the intensity of thermal radiation received by the PbS detector, which is represented by the voltage output in Eq. (3.3). The blackbody used in calibration emits theoretically the highest level of intensity. Therefore, the one-color method tends to under-estimate the temperature. The two-color method does not rely on the intensity for measurement and may over- or under-estimate the temperature due to the variation in emissivity  $\varepsilon(\lambda)$  and transmissivity  $\tau(\lambda)$ . In general, the two-color method predicts higher temperature than the one-color method, except at fiber tip location IS after 120 s.

For the low temperature measurement below 150°C, the one-color method is able to acquire temperature between 100 to 150°C. However, due to the steep slope of the calibration curves in Fig. 3.7, the accuracy of the measured temperature below 150°C is poor. The two-color method can measure low temperatures in Cavity I with results closely matched to that obtained with the one-color method. In Cavity II, the two-color method fails to measure temperature below 150°C. This is due to the low  $V_{PbSe}$  output at low temperatures in Cavity II. The large cavity size limits the emissivity enhancement within that cavity and the

radiation intensity received by the PbSe detector for the two-color low temperature measurement.



(a)



(b)

Figure 3.11. Temperature vs. time at four locations during microwave heating tests.

### 3.7. Low Temperature Measurement Capability Improvement

Theoretical calculations show the low temperature sensing limit of PbS and PbSe detectors can be as low as room temperature [11]. Due to signal attenuation in the long and thin sapphire fiber, the limit of low temperature is about 100°C for the near blackbody, large aspect-ratio cavity. Using the lock-in amplifier for both infrared detectors and increasing the gain of the PbSe detector, the low temperature measurement capability can be further improved to observe the filter warm-up. To demonstrate this concept and explore the low temperature measurement capability of the system, a lock-in amplifier was added between the output of the PbS channel and the input of the data acquisition system. The system configuration is shown in Fig. 3.12. The lock-in amplifier samples the frequency of the mechanical chopper as a frequency reference to provide high-resolution signal output.

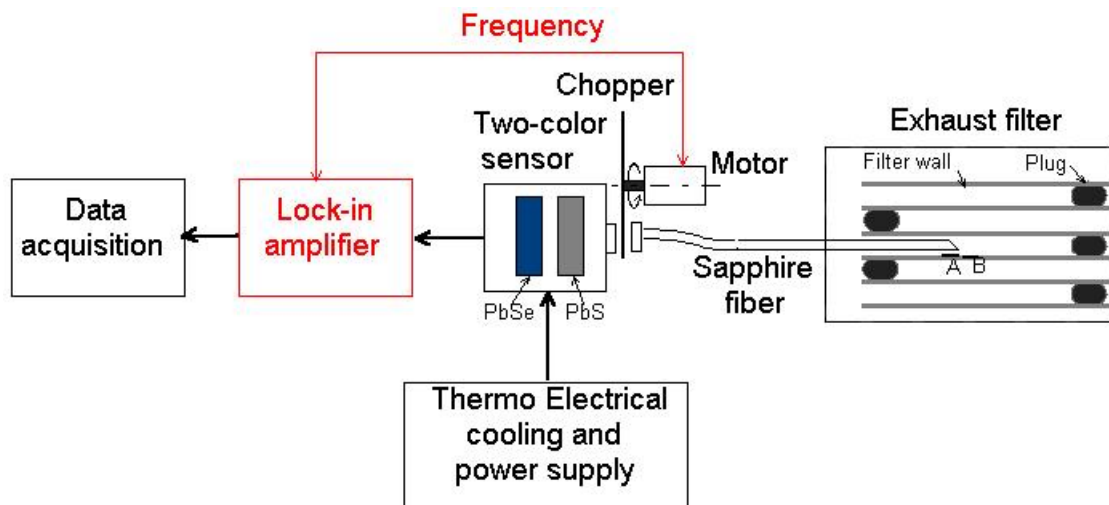


**Figure 3.12. The application of lock-in amplifier for improvement of low temperature measurement capability**



The system was then calibrated against the blackbody heat source as described in Sec. 3.4. The calibration test was conducted from 50°C to 320°C. Beyond the temperature of 320°C, the lock-in amplifier was saturated. A set of calibration data points and a polynomial fitting curve are shown in Fig. 3.13. The calibration curve shows good sensitivity down to a temperature about 70°C, which is 80°C lower than the 150°C, the turn point of the calibration curve in Fig. 3.7(a). The calibration curve can be expressed as:

$$T = 0.48 [\ln(V_{Pbs})]^3 - 3.72 [\ln(V_{Pbs})]^2 + 41 [\ln(V_{Pbs})] + 194.75 \quad (70^\circ\text{C} < T < 320^\circ\text{C}) \quad (3.7)$$

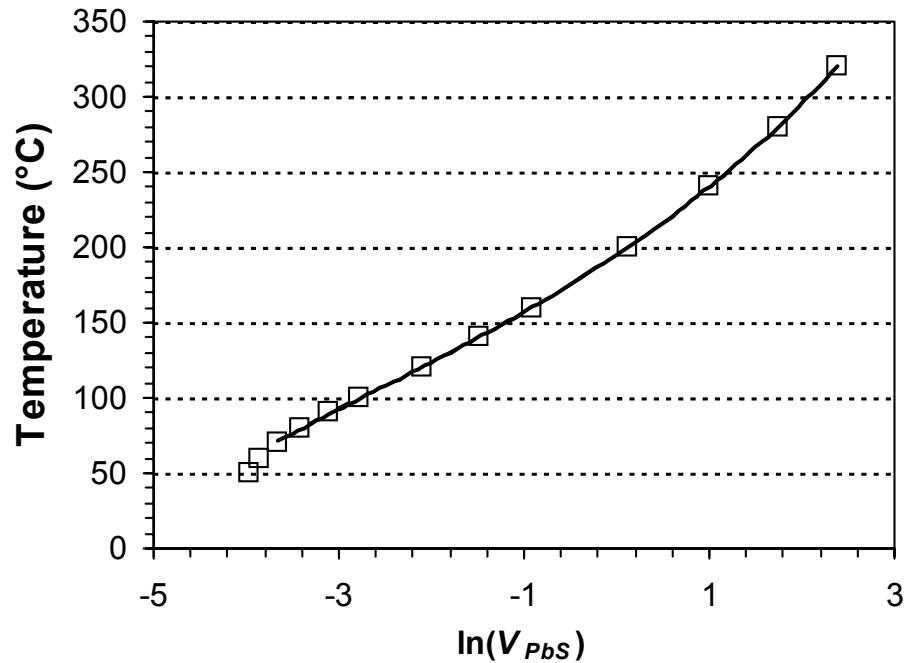


**Figure 3.13. Blackbody calibration result of PbS channel with a lock-in amplifier**

Fig. 3.14 shows the temperature vs. time results calculated from one-color without lock-in amplifier, two-color, and one-color with lock-in amplifier at the same location in a diesel particulate filter during microwave heating. It can be seen that the temperature results

measured by the three methods closely match each other when the temperature is above 150°C. The one-color method using lock-in amplifier reported a steady increasing temperature history starting from about 80°C.

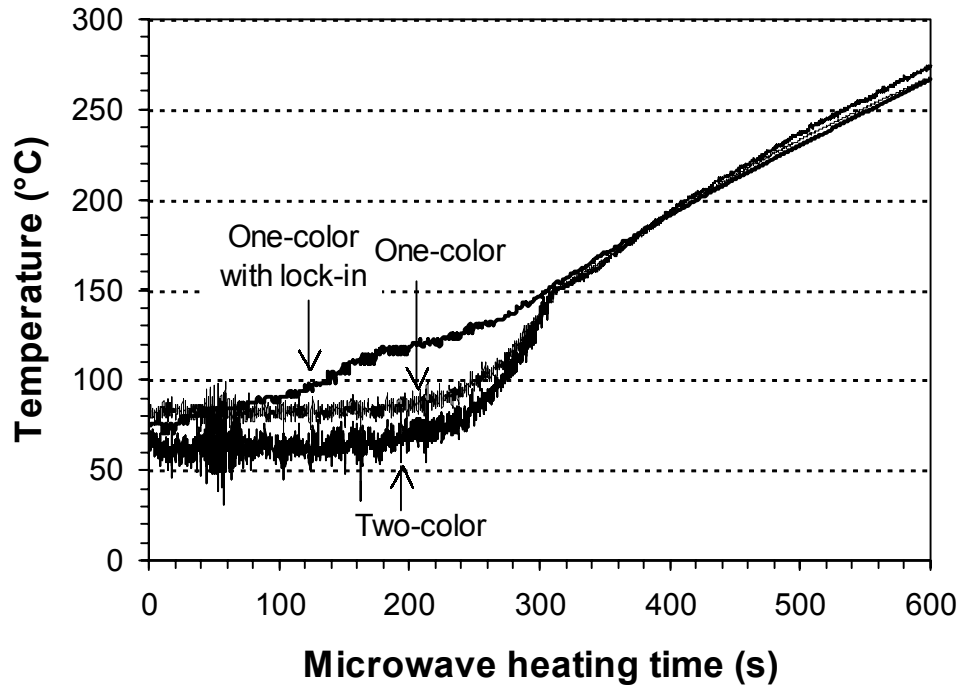


**Figure 3.14. Temperature vs. time results of one-color method w/o lock-in amplifier and two color method**

### 3.8. Parasitic Heating Effect

During temperature measurement, the thin sapphire fiber tends to deflect and lay on the hot filter wall surface. The filter wall surface temperature in contact with the fiber may be higher than the region observed by the fiber tip. Kottmann and Stenzel [17] have studied the scattered or parasitic light effect and demonstrated that the scattered light has insignificant effect on flexible sapphire fibers for high temperature measurement. For low

temperature measurement, the scattered light effect may have more noteworthy impact due to the lower intensity of spectral emission from the low temperature target. It is assumed that the thermal radiation signal from the fiber tip is not affected by other high temperature thermal radiation sources along the fiber. An experiment was designed to validate the assumption used in this study.

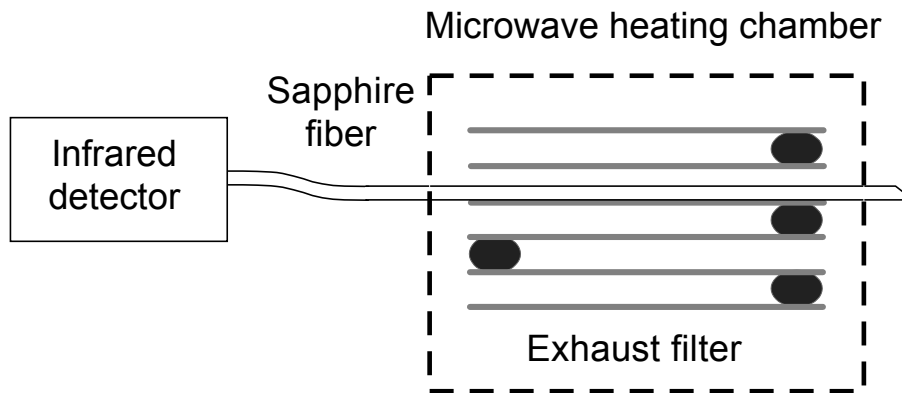


**Figure 3.15. Experiment setup to test the scattered light around the fiber.**

The setup of the experiment is shown in Fig. 3.15. The fiber penetrated through Cavity I (Fig. 3.9) and was laying on the cavity surface. The filter was heated for 240 s using the same setup as in the temperature measurement tests described in Sec. 4. During microwave heating, the sapphire fiber was subject to an electromagnetic field. The hot, over 400°C, filter surface was in contact with the fiber. The fiber tip was exposed to the dark room background temperature, which does not generate detectable sensor output. The sensor output voltages were recorded. The PbS and PbSe detectors have less than 1.25% and 2% change in output voltage, respectively, when compared to the voltage output in the

temperature measurement tests. This indicates that the scattered light from the fiber surrounding does not affect the temperature measurement.

This experiment further proves that sapphire fibers can be used for low temperature measurement and the effect of scattered light is not significant.

### **3.9. Concluding Remarks**

A fiber optic radiation thermometry system was developed to measure the channel wall surface temperature in a diesel exhaust aftertreatment filter. Based on two wide-band infrared PbS and PbSe detectors, the system is able to measure temperatures ranging from 100 to 400°C in the filter channel with large aspect ratios. By employing a sapphire fiber with 45° angled tip, the thermal radiation from a small and specific region opposite the polished tip face and perpendicular to the fiber axis can be measured. Both one-color and two-color thermometry methods were implemented in this study. The two-color method generally predicted higher temperature than the one-color method. The discrepancy between the two temperature measurement methods was small for the channel with large aspect ratio or near blackbody characteristics. Experimental results show that the system is suitable for the non-contact, in-situ temperature measurement for diesel exhaust aftertreatment filters.

With a lock-in amplifier the low temperature measurement capability of the sensor was further improved. Experimental results show the sensor is able to measure the temperatures as low as 70°C to 80°C.

On-going research of the development is to implement this system in an operating diesel exhaust aftertreatment filter with exhaust flow, soot deposition, and coated catalysts.

The filter will be subject to hot exhaust gas and experience temperature cycling while capturing and regenerating the NO<sub>x</sub> or particulates.

### References

- [1] A.G. Konstandopoulos, M. Kostoglou, E. Skaperdas, E. Papaioannou, D. Zarvalis, and E. Kladopoulou, 2000, "Fundamental Studies of Diesel Particulate Filters: Transient Loading, Regeneration and Aging," SAE 2000-01-1016.
- [2] F.B. Walton, P.J. Hayward, and D.J. Wren, 1990, "Controlled Energy Deposition in Diesel Particulate Filters During Regeneration by Means of Microwave Irradiation," SAE 900327.
- [3] B.J. Boothe, A.J. Shih, J. Kong, and W.L. Roberts, 2003, "Goniometric Characteristics of Optical Fibres for Temperature Measurement in Diesel Engine Exhaust Filters," *Measurement Science and Technology*, Vol. 14, No. 5, pp. 563–572.
- [4] A. Mayer, T. Lutz, C. Lammle, M. Wyser, and F. Legerer, 2003, "Engine Intake Throttling for active Regeneration of Diesel Particle Filters," SAE 2003-01-0381.
- [5] H. Okazoe, K. Shimizu, Y. Watanabe, W. Santiago, P. Kugland, and W. Ruth, 1996, "Development of a Full-Flow Burner Regeneration Type Diesel Particulate Filter Using SiC Honeycomb," SAE 960130.
- [6] B. Terry and P. Richards, 2000, "A Method for Assessing the Low Temperature Regeneration Performance of Diesel Particulate Filters and Fuel-borne Catalysts," SAE 2000-01-1922.
- [7] A.E. Awara, C.N. Opris, and J.H. Johnson, 1997, "A Theoretical and Experimental Study of the Regeneration Process in a Silicon Carbide Particulate Trap Using a Copper Fuel Additive," SAE970188.
- [8] A. Pfeifer, M. Krueger, U. Gruetering, and D. Tomazic, 2003, "U.S. 2007-Which Way to Go? Possible Technical Solutions," SAE 2003-01-0770.
- [9] H.L. Fang, S.C. Huang, R.C. Yu, C.Z. Wan, and K. Howden, 2002, "A Fundamental Consideration on NO<sub>x</sub> Adsorber Technology for DI Diesel Application," SAE 2002-01-2889.
- [10] P., Klocek, 1991, *Handbook of Infrared Optical Material*, Marcel Dekker, New York, pp. 198.

- [11] D.P. Dewitt and G.D. Nutter, 1989, *Theory and Practice of Radiation Thermometry*, John Wiley & Sons, pp. 21–52 and 231–337.
- [12] E.L. Dereniak and D.G. Crowe, 1984, *Optical radiation detectors*, John Wiley & Sons, pp. 86–106.
- [13] K.A. Wickersheim, 1992, “Fiberoptic Thermometry: An Overview,” *Temperature, Its Measurement and Control in Science and Industry*, J. F. Schooley (Ed.), the 7th International Temperature Symposium, Toronto, Ontario, Canada, Apr. 28–May 1, 1992, American Institute of Physics, Vol. 6, pp. 711–714.
- [14] J.C. Richmond, D.P. Dewitt, and W.D. Hayes, 1964, “Procedures for the Precise Determination of Thermal Radiation Properties November 1962 to October 1963,” National Bureau of Standards Technical Note 252, Nov. 20.
- [15] R.F. Gansman, 1991, “Using Reflection Measurement to Calculate Emissivity for Improved In-Situ Temperature Measurement in Rapid Thermal Processing,” *MS Thesis, North Carolina State University*.
- [16] R.D. Nixdorf, “Filter and Means for Regeneration thereof,” US Patent 5,087,272.
- [17] J. Kottmann and C. Stenzel, 1999, “Characterization of Flexible Sapphire Fibers in High-Temperature Pyrometers,” *Sensors and Materials*, Vol. 11, No. 4, pp. 233–246.

## **CHAPTER 4. INFRARED THERMOMETRY MEASUREMENT OF TEMPERATURE DISTRIBUTION IN MICROWAVE REGENERATION OF DIESEL PARTICULATE FILTERS**

### **4.1. Introduction**

Particulate Matter (PM) is one of the major pollutants in diesel engine emissions. Over the years, progressively reducing the PM emission towards clean diesel engine, as regulated by worldwide environmental protection agencies, has been achieved through engine development and fuel reformulation [1]. The US 2007, EURO IV, and Japan 2005 PM standards [2] demand a significant reduction of PM emission. This has accelerated the development of diesel particulate aftertreatment technology. Diesel particulate filter (DPF) is used in the aftertreatment process to capture the PM in diesel exhaust. Periodical filter regeneration is required to clean the filter by burning or oxidizing the stored PM. To lower the PM regeneration temperature, catalyst technology is applied via either coating [3] or fuel additive [4,5]. Several filter regeneration techniques have also been developed, including the fuel burner [6,7], electrical heater [8], engine thermal management [9], and microwave heating [10-14]. A review has been summarized by Johnson [2].

The unique selective and inner heating nature of microwave makes it attractive over conventional heating means. The system is useful in the harsh environment of exhaust aftertreatment system. A number of studies on fundamental aspects of microwave regeneration, such as the development and selection of filter media and geometric configuration, design of cavity and microwave heating system, microwave power level and

heating duration, regeneration efficiency, and catalyst effect, have been investigated [10-15]. A review has been given by Gautam et al. [12].

The temperature at filter walls in DPF controls the chemical kinetics of the storage and regeneration processes. A uniform temperature distribution is critical to controlling the homogeneous chemical reactions as well as avoiding the thermal stress fatigue and overheating of the filter. However, microwave heating is usually not uniform. During the heating, hot and cold spots are generated due to peaks and valleys of the electromagnetic field distribution. This can possibly be compensated by the optimization of filter material composition, filter geometry design, and heating cavity design. Walton et al. [11] has successfully obtained a uniform filter inlet temperature of  $185 \pm 15^\circ\text{C}$  by replacing the end-plugs of a wall flow filter with the ferrite/cordierite composite material. SiC reacts quickly and efficiently in microwave to generate heat. The addition of SiC in the DPF can make the temperature distribution in DPF during microwave heating independent of the PM loading [14]. Realizing uniform temperature distribution is a key step for reliable and successful microwave regeneration of DPF.

The DPF has deep channels to increase the specific surface area. Accurate temperature measurements of a small and specific region on the filter wall can provide important information to chemical engineers for the catalytic development, material engineers for the filter development, and mechanical engineers for the design of the filter regeneration process. Attaching traditional thermocouples to the porous ceramic wall at locations deep in the filter is difficult due to the space constraint. The harsh environment in the filter, which is subject to high temperature airflow from the engine combustion and thermal cycling as a consequence of periodical regeneration, also makes the connection of



thermocouple tip to filter wall surface technically challenging. If microwave heating is used, the application of thermocouple is prohibited due to its metallic composition, which distorts the electromagnetic field distribution and hence the heating profile in DPFs. Researchers typically apply thermocouples, during microwave regeneration, to measure the air temperatures at the filter inlet and outlet, or the surface temperatures of filter inlet, outlet and filter can, to estimate the temperature profile in DPF [12,13].

In this study, silica light-pipes were employed to collect emitted radiation from the inside wall surfaces of DPFs. The radiation from a small and specific region of the inner filter wall surface can be detected. Temperature is calculated by a one-color infrared transducer (Mikron M680). Components and features of the multi-channel fiber optic temperature measurement and microwave heating systems are first introduced. Temperature measurement calibration and validation are subsequently presented. Results from the in-situ temperature measurement experiments performed on three DPFs are then analyzed and discussed.

## **4.2. System Component Description**

The infrared fiber optic temperature measurement and microwave heating systems are discussed in the following two sections.

### **4.2.1. Multi Channel Infrared Fiber Optic Temperature Measurement System**

The multi channel infrared fiber optic temperature measurement system, provided by Mikron Instrument Inc., consists of the M680 thermometer, silica light-pipe, transmission fiber, and control software. The M680 thermometer utilizes multiple embedded processors to

provide four channels of temperature data acquisition. For each channel, target infrared radiation is collected by a silica light-pipe and transmitted to the thermometer through a transmission fiber, as shown in Fig. 4.1. In this study, four channels of the M680 thermometer are used to simultaneously measure the temperature at different locations in DPF.

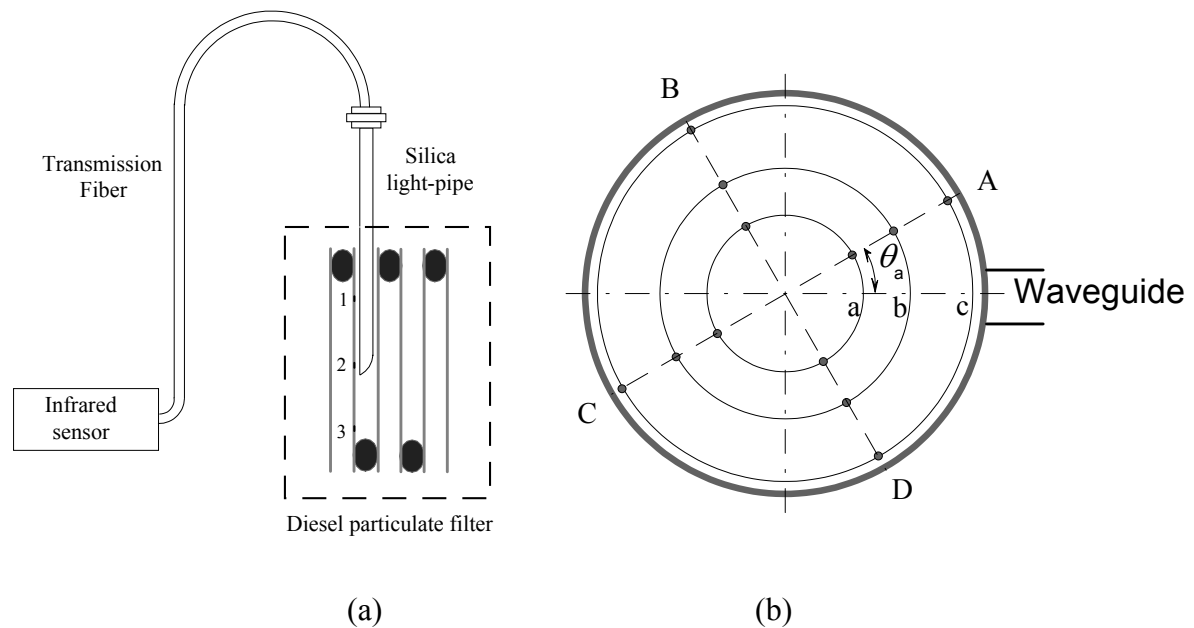


**Figure 4.1. Experimental setup of multi channel infrared fiber optic sensor for the measurement of diesel exhaust aftertreatment filter temperature; (a) cross-sectional view and (b) top view of the optical fiber insertion locations.**

The silica light-pipe is 300 mm long and 2 mm in diameter. Four light pipes are inserted to the small, deep channels in DPF. As shown in Fig. 4.2, the tip of the light-pipe is bent and polished to have a flat surface parallel with the optical axis. This tip geometry enables the light-pipe collect the infrared radiation in two directions in front of the tip [16].

The transmission fiber is a glass fiber sheathed with stainless steel. The fiber is 3.65 m long and 1 mm in diameter with SMA connectors on both ends. The silica material is transparent to microwaves. During microwave heating, the silica light pipes are immune and also have no distortion to the applied electromagnetic field.

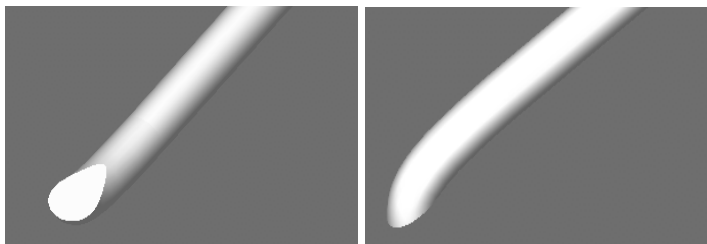


**Figure 4.2. Silica light-pipe with bent and polished tip.**

The semiconductor detector material used in the M680 thermometer is InGaS, which provides good sensitivity to near infrared radiation in a spectral band of 1.0 – 1.6  $\mu\text{m}$ . Both the silica light-pipe and transmission fiber are transparent in this spectral band. This system is able to measure temperature from 150 to 1000°C, which makes it suitable for the observation of a wide temperature variation due to exothermic reaction in the DPF regeneration process. This multi-channel one-color (single wavelength) infrared thermometer system has an accuracy of 1.0°C and a repeatability of 0.2°C, as specified by the manufacturer.

#### **4.2.2. Microwave Heating System**

The microwave heating system was setup to study the heating effect on different operating conditions and filter materials. The system includes the power supply, microwave

generator, coupler, microwave power meters, isolator/waterload, tuner, waveguide, and microwave cavity. The configuration of the microwave heating system is illustrated in Fig. 4.3. A system would include only the generator, microwave cavity, waveguide, and power supply for the engine application.

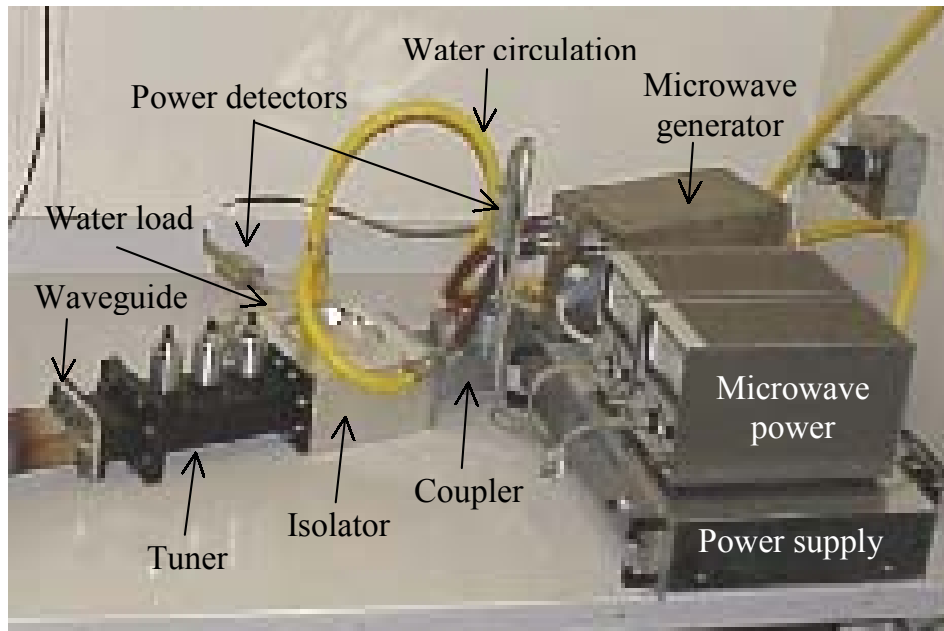


**Figure.4.3. Overview of the developed bench scale microwave heating system.**

The maximum microwave power output is 2 kW. Adjustable power output helps to determine the power level required in different engine operating conditions. During heating, the forward microwave power is monitored by a power meter. The reflected microwave power from the waveguide is diverted by the isolator to a water load, where the microwave energy is converted to heat and carried away by the circulating water. This eliminates the effect of backward power on microwave generator. The level of backward power is

monitored by a power meter and adjusted through a tuner. This ensures that majority of the microwave output energy is directed to the microwave cavity.

### **4.3. Temperature Measurement Calibration and Validation**

The temperature measurement calibration and validation to demonstrate the feasible use of one-color radiation thermometry method, the opaqueness of the filter material and repeatability of the microwave heating and infrared temperature measurement are discussed.

#### **4.3.1. One-Color Temperature Measurement Calibration**

As shown in Fig. 4.1, the DPF have deep channels to increase the specific surface area. The length to width ratio of a channel is typically over 30. The porous ceramic filter wall surface is also a good diffuse emitter. Both of these characteristics make it suitable to approximate the filter cavity as a blackbody [17]. With this simplification, the emissivity is assumed as 1.0 and a blackbody heat source, as described in [17], is used to calibrate the system.

#### **4.3.2. Filter Material Opaqueness Test**

Proprietary ceramic wall flow DPFs were used in this study. Since filter channels are adjacent to each other, the opaqueness of filter wall in 1.0–1.6  $\mu\text{m}$  wavelength range needs to be studied to ensure that infrared signals from other channels will not affect the temperature measurement results.

A test was conducted by putting a small piece of the filter material to cover the receiving end of the M680 thermometer. A heat source with strong radiation in the 1.0–1.6

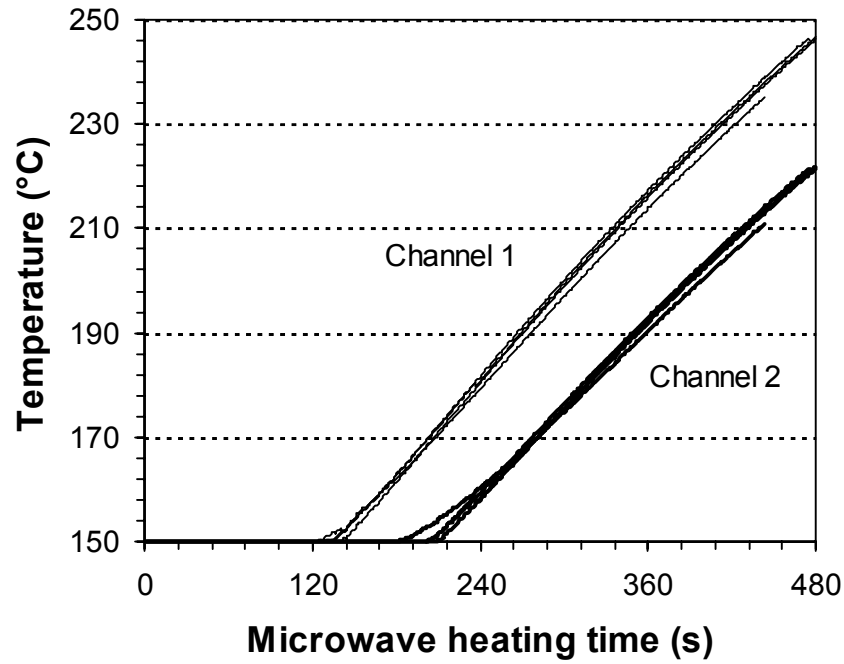
$\mu\text{m}$  infrared spectral band was placed and oscillating in front of the filter material. Under this setup, the M680 thermometer cannot detect any infrared signal transmitted through the filter. This demonstrated the opaqueness of the filter material and the feasibility to use the experiment setup outlined in Sec. 2.1 to measure the temperature distribution in DPF.

### 4.3.3. Filter Heating Repeatability Tests

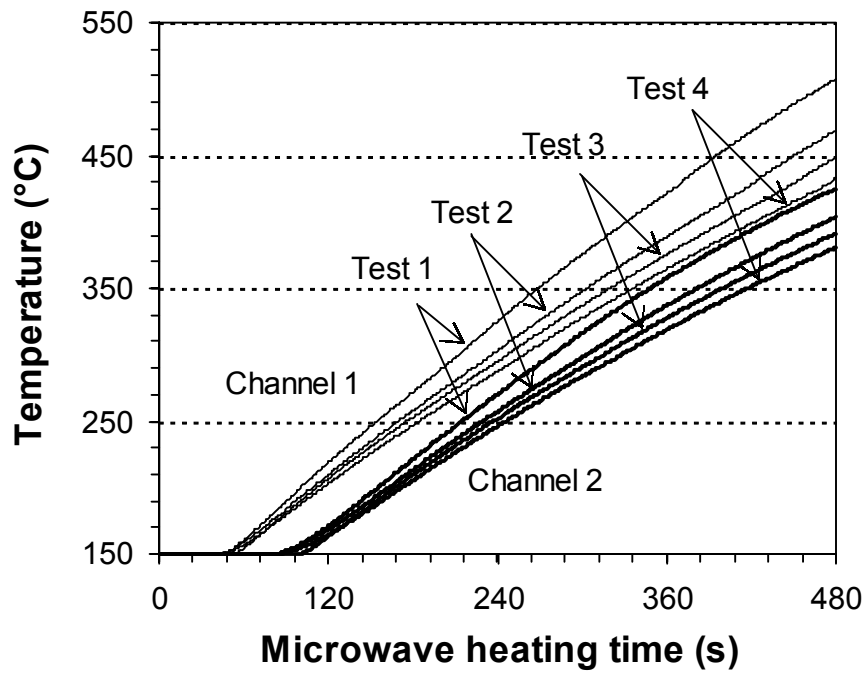
The mapping of temporal and spatial temperature distribution in DPF was achieved by measuring the surface temperature at 36 locations inside filter channels. Only four silica light pipes were available for temperature measurement in each test. To demonstrate repeatable filter temperature distribution during microwave heating, four microwave heating tests with temperature measurement at two locations in a DPF was conducted. Identical microwave heating setups were used in each test. Before starting each microwave heating test, the DPF was cooled to the room temperature.

Fig. 4.4 shows the temperature results at two locations, marked as Channels 1 and 2, in a DPF under 500 and 1000 W microwave power output in four repeated tests, denoted as Test 1, 2, 3, and 4. The microwave heating time was 480 s for each test. The temperature has good repeatability at both locations under 500 W power level. At the 1000 W power level, the temperature progressively becomes lower after each test. This trend of lowering temperature occurs at both filter locations. The largest discrepancy of temperature between Tests 1 and 4 was about 80°C at Channel 1 and 50°C at Channel 2. The lowering temperature is likely caused by the reaction of microwave absorbing components at high temperature under 1000 W microwave heating. Based on this observation, all tests conducted for mapping the temperature distribution in DPF were set up under 500 W power

level unless the heating under the 500 W was not adequate to increase the temperature at an satisfactory rate.



(a)



(b)

**Figure 4.4. Results of temperature heating repeatability tests; (a) repeatable temperature curves at 500 W microwave power setting and, (b) unrepeatabile temperature curves at 1 kW microwave power setting.**



#### 4.4. Filter Heating and Temperature Measurement Experimental Setup

Fig. 4.5 shows the setup for temperature measurement in a DPF 152 mm long and 152 mm in diameter. The overall setup combines both the microwave heating system (Fig. 4.3) and temperature measurement system. Silica light-pipe is very brittle and can withstand little bending. A fixture with three translational degrees of freedom was used to facilitate the insertion and positioning the tip of the light-pipe in the DPF. A cover plate with an array of drilled 6 mm diameter through holes (Fig. 4.5(b)) was manufactured to assist locating the light-pipes to a specific channel in the filter. The holes were small enough that no microwave leakage was detected with a HP 435B power meter.

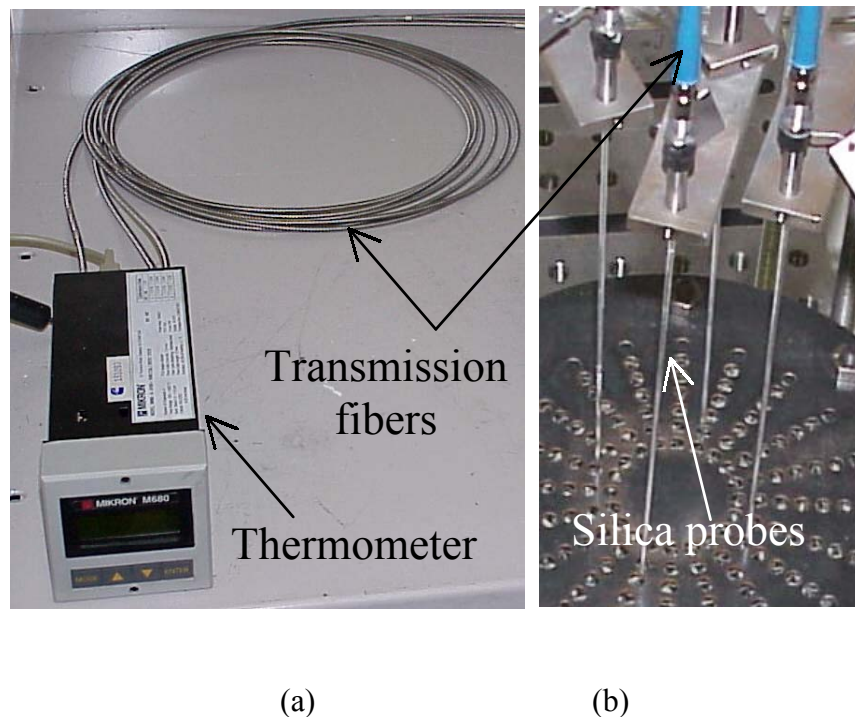


**Figure 4.5. Setup for microwave heating temperature measurement; (a) Thermometers and transmission fibers (b) close-up view of the silica light-pipes insertion.**

As shown in Fig. 4.1, the tip of light pipe is located in three radial, three axial, and four angular orientations. In total, 36 ( $=3 \times 3 \times 4$ ) tip locations were used to map the temperature distribution in the DPF. Three axial heights are marked as 1, 2, and 3, which are 25, 75, and 125 mm from the filter face, respectively. The three radial positions are designated as a, b, and c, which are at a radius of 35, 50, and 75 mm from the filter center axis, respectively. The four angular locations are represented by A, B, C, and D, at an angle of  $30^\circ$ ,  $120^\circ$ ,  $210^\circ$ , and  $300^\circ$  from the waveguide direction, as shown by  $\theta_a$  in Fig. 4.1. At each location, the temperature measurement test was repeated for three times and the results were averaged. A total of 108 ( $=36 \times 3$ ) temperature measurements were performed on each DPF. A sign convention is developed to use three consecutive letters in the order of radial position, height, and angular orientation to identify the temperature measurement position in the filter. For example, a3B represents the optical fiber tip location at radial position a, height level 3, and angular orientation B inside the filter.

Each microwave heating test lasted 600 s. The sampling rate of temperature data was set at 60 points/s. After each heating test, the filter was cooled to room temperature without removing from the microwave heating system. A thermocouple was used to ensure that the DPF temperature had been reduced to room temperature.

#### 4.5. Temperature Measurement Results and Discussion

Three advanced wall-flow DPFs were tested. These DPFs are designated as F1, F2, and F3, which are the uncatalyzed filter with soot loading, catalyzed filter without soot loading, and catalyzed filter with soot loading, respectively. Temperature measurement results of these three filters are discussed in the following three sections.

#### 4.5.1. Filter F1 -- Uncatalyzed Filter with Soot Loading

Fig. 4.6 shows the measured temperature of filter F1. The three rows represent the three heights of the fiber tip locations 1, 2, and 3, as shown in Fig. 4.1(a). The two columns represent the two radial positions a and b, as shown in Fig. 4.1(b). The temperature in radial position c, outer portion of the filter, was too low to be recorded during microwave heating. This demonstrates that the heating across the filter is not uniform. In general, the temperature at the top and outer area of the filter is lower than in the bottom and inner area. The temperature increases progressively from height 1 to 3, i.e., lower portion of the filter is heated more rapidly. In the radial direction, the temperature is higher near the center (a). The highest temperature occurs at the position a3C, the inner bottom area away from the waveguide (see Fig. 4.1(b) for angular orientation C). No temperature above the sensor lower limit 150°C can be detected at many locations in the outer and top areas. For example, only three locations at height 1 (a1C, b1C, and b1D in row 1 in Fig. 4.6) show temperatures above 150°C. Temperatures at height 2 (b2C and b2D) are higher than at height 1 and 3 (b1C, b1D, b3C, and b3D). This shows that in the center section of the filter is heated more rapidly than the top and bottom (heights 1 and 3). This heating pattern has been used to validate the results obtained from electromagnetic modeling of microwave heating with good agreement.

The discrepancy in heating rate across the filter surface generates non-uniform temperature distribution and chemical reaction for regeneration. The temperature gradient in the filter can also create thermal stresses and thermal cycle fatigue problem. Measured temperatures are the base for the analysis of these filter reliability and durability issues.

Another interesting feature recognized in Fig. 4.6 is the variation of temperatures to the angular orientation effect. Temperatures are in the order of C (away from the waveguide), B, D, and A (close to the waveguide) from high to low. The temperature difference is about 40°C between a3C and a3A. All temperatures at angular location A are low, below the 150°C limit other than a3A. To further confirm this angular non-symmetry heating characteristic, the filter was turned 180° and then heated by the microwave under the same setup. The same non-symmetry pattern matching to results shown in Fig. 4.6 was obtained. The cavity design is the likely cause for the angular non-symmetry heating characteristic.

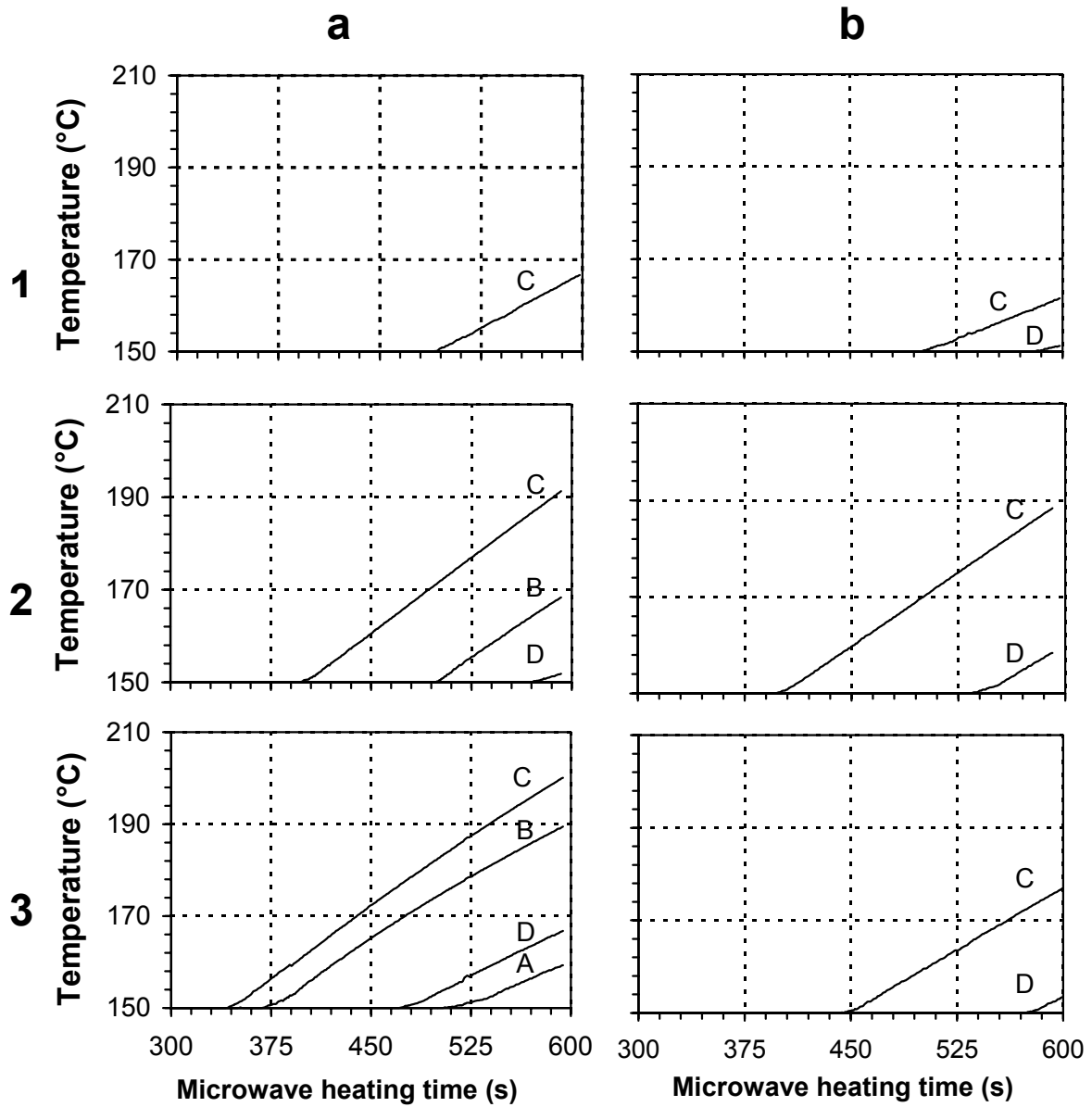


Figure 4.6. Temperature vs. time results at 36 locations in filter F1 during microwave heating tests.

#### 4.5.2. Filter F2 -- Catalyzed Filter without Soot Loading

Fig. 4.7 shows the temperature measurement results of filter F2, a catalyzed filter without soot loading. Microwave heating at 500 W was first tested. The temperature was very low and the power input was increased to 1 kW. The slow heating was due to the catalyst coating applied to the filter, which increased thermal mass and required more heat input. At this power setting, the repeatability of temperature distribution still holds.

Comparable pattern of temperature distribution as in filter F1 (Fig. 4.6) was observed. The highest temperature occurred at location a3C. Column c, which represents the outer most radial position, was not heated to above 150°C. Temperature at top, height 1, of the filter is generally lower than the bottom. Nevertheless, some differences can be identified in Fig. 4.7. The temperature distribution is more uniform than in filter F1. Temperatures at two more locations, a1D and b1B, at height 1 (row 1 in Fig. 4.7) are beyond the sensor detectable limit of 150°C. Temperature curves at a2B, a2C, and a2D are closer to each other. Temperature differences among three locations at height 3, a3B, a3C, and a3D, are within a deviation of 15°C. Comparing temperatures at different heights in radial position b, as shown by column b in Fig. 4.7, temperatures in cavities bB and bD show the similar pattern as in filter F1: high in the center (b2B and b2D) of the cavity. However, no significant temperature differences can be observed in the cavity bC.

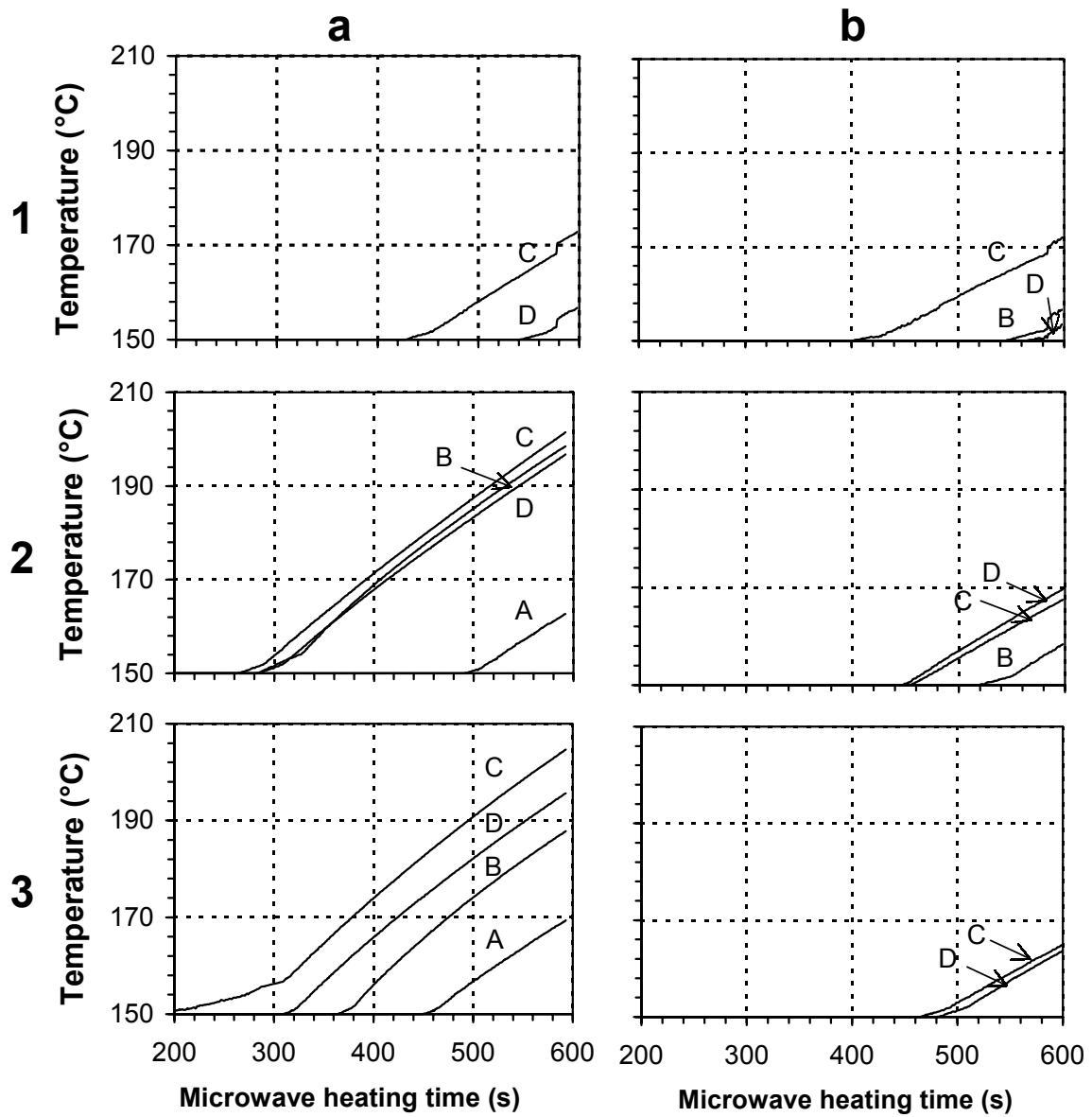


Figure 4.7. Temperature vs. time results at 36 locations in filter F2 during microwave heating tests.

### 4.5.3. Filter F3 -- Catalyzed Filter with Soot Loading

The temperature measurement results of filter F3, a catalyzed filter with soot loading, is shown in Fig. 4.8. The microwave power setting (1 kW) is the same as to filter F2 in order to compare the heating pattern between these two filters. Temperatures at column c, the outside radial locations, can now be detected.

Temperatures are much higher in filter F3 than in F2. Temperatures at most locations, after 600 s of microwave heating, are beyond 200°C, comparable to the highest temperature reached in filter F1 and F2. The highest temperature of 420°C, as shown by b1C and b1D in Fig. 4.8, is twice higher than the highest temperature in filters F1 and F2. The highest temperature at b1C and b1D occurs at the top of the filter (height 1), not in the bottom of the filter as in F2 and F3. For example, temperatures at a1A, a1B, a1C, and a1D are all higher than those at a2A, a2B, a2C, and a2D and a3A, a3B, a3C, and a3D, respectively. This is different from the heating pattern observed in filters F1 and F2.

The interaction between catalyst coating, soot loading, and microwave accounts for the high temperatures generated and heating pattern change in filter F3. Soot itself has high dielectric constant  $\epsilon''=7.4$  [13] and is a strong microwave absorber. The soot loading is more concentrated in the top than the bottom of the filter F3. This contributes to the higher temperatures at height 1.

The radial non-symmetry of temperature distribution still exists in filter F3. Temperatures in angular locations A (close to the waveguide) are the lowest among all the 4 angular locations. This problem could be abated using improved cavity design.



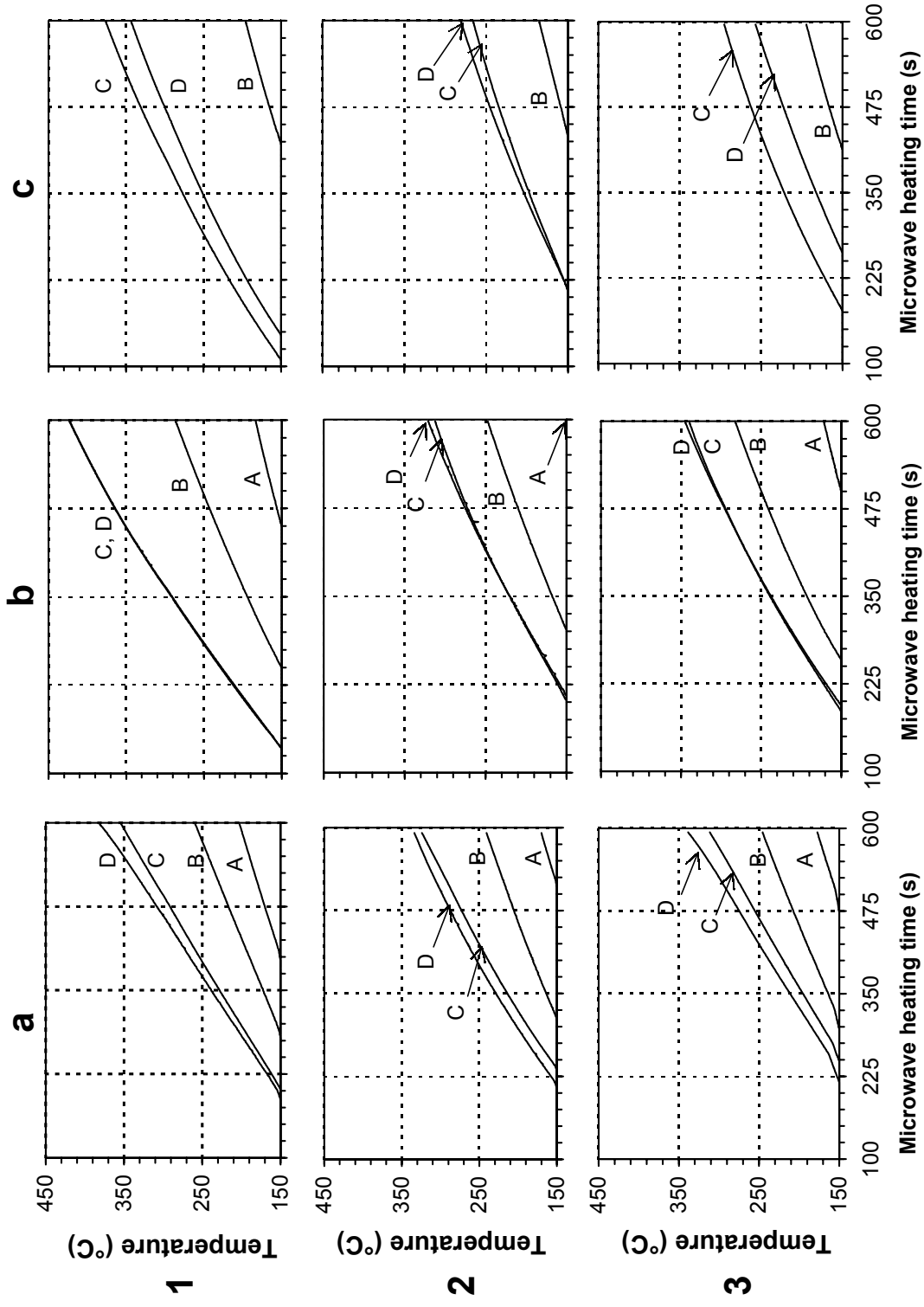


Figure 4.8. Temperature vs. time results at 36 locations in filter F3 during microwave heating tests.

#### 4.6. Concluding Remarks

Infrared thermometry method was applied to study of temperature distribution in microwave assisted diesel particulate filter regeneration. Temperature measurement tests were performed by the integration of a multi channel fiber optic infrared temperature measurement system and a microwave heating system. Instead of thermocouples, Silica light-pipes, which are transparent to the microwave electromagnetic field, are used to collect infrared radiation inside filter cavities.

Three advanced DPFs were heated with microwaves and, the measured temperature profiles were studied. Experimental results show non-uniform heating across the filter. The temperature distribution in these filters was similar to modeling results. The interaction between catalyst, soot loading, and microwave power changes the heating pattern and temperature level. During a 600 s heating period, a 1 kW microwave power setting was able to raise the temperatures above 200°C in most area of a catalyzed filter with soot loading.

The temperature profiles obtained in this study have provided important data for filter materials and cavity development to further reduce temperature gradients during microwave assisted DPF regeneration.

#### References

- [1] R. Mital, J. Li, S.C. Huang, B.J. Stroia, R.C. Yu, J.A. Anderson, and K. Howden, 2003, "Diesel Exhaust Emissions Control for Light Duty Vehicles," SAE2003-01-0041
- [2] T.V. Johnson, 2003, "Diesel Emission Control in Review - The Last 12 Months," SAE2003-01-0039

- [3] R. Allansson, P.G. Blakeman, B.J. Cooper, H. Hess, P.J. silcock, and A.P. Walker, 2002, "Optimizing the Low Temperature Performance and Regeneration Efficiency of the Continuously Regenerating Diesel Particulate Filter (CR-DPF) System," SAE2002-01-0428
- [4] B. Terry and P. Richards, 2000, "A Method for Assessing the Low Temperature Regeneration Performance of Diesel Particulate Filters and Fuel-borne Catalysts," SAE 2000-01-1922
- [5] A.E. Awara, C.N. Opris, and J.H. Johnson, 1997, "A Theoretical and Experimental Study of the Regeneration Process in a Silicon Carbide Particulate Trap Using a Copper Fuel Additive," SAE970188
- [6] H. Okazoe, K. Shimizu, Y. Watanabe, W. Santiago, P. Kugland, and W. Ruth, 1996, "Development of a Full-Flow Burner Regeneration Type Diesel Particulate Filter Using SiC Honeycomb," SAE 960130
- [7] D.S. Park, J.U. Kim, H. Cho, and E.S. Kim, 1998, "Considerations on the Temperature Distribution and Gradient in the Filter During Regeneration in Burner Type Diesel Particulate Trap System (II)," SAE980188
- [8] J. Kitagawa, T. Hijikata, and S. Yamada, 1991, "Electric Heating Regeneration of Large Wall-Flow Type DPF," SAE910136
- [9] O. Salvat, P. Marez, and G. Belot, 2000, "Passenger Car Serial Application of a Particulate Filter System on a Common Rail Direct Injection Diesel Engine," SAE2000-01-0473
- [10] C.P. Garner, and J.C. Dent, 1989, "Microwave Assisted Regeneration of Diesel Particulate Traps," SAE890174
- [11] F.B. Walton, P.J. Hayward, D.J. Wren, 1990, "Controlled Energy Deposition in Diesel Particulate Filters During Regeneration by Means of Microwave Irradiation," SAE900327
- [12] M. Gautam, S. Popuri, B. Rankin, and M. Seehra, 1999, "Development of A Microwave Assisted Regeneration System for A Ceramic Diesel Particulate System," SAE1999-01-3565
- [13] M. Henrichsen and S. Popuri, 2001, "Development of A Microwave Assisted Particulate Filter Regeneration System," 7<sup>th</sup> Diesel Engine Emissions Reduction (DEER) Workshop, August 5-9, 2001

- [14] R.D. Nixdorf, J.B. Green Jr., J.M. Story, and R.M. Wagner, 2001, "Microwave-Regenerated Diesel Exhaust Particulate Filter," SAE2001-01-0903
- [15] J. Ma, M. Fang, P. Li, B. Zhu, X. Lu, and N.T. Lau, 1997, "Microwave-assisted Catalytic Combustion of Diesel Soot," *Applied Catalysis A: General*, Vol. 159, No. 1-2, pp. 211-228
- [16] B.J. Boothe, A.J. Shih, J. Kong, and W.L. Roberts, 2003, "Goniometric Characteristics of Optical Fibres for Temperature Measurement in Diesel Engine Exhaust Filters," *Measurement Science and Technology*, Vol. 14, No. 5, pp. 563–572
- [17] J. Kong and A.J. Shih, "Infrared Thermometry for Diesel Exhaust Aftertreatment Filter Temperature Measurement," SAE Transactions (submitted)
- [18] D.P. Dewitt and G.D. Nutter, 1989, *Theory and Practice of Radiation Thermometry*, John Wiley & Sons, pp. 21–52

## CHAPTER 5. CONCLUSIONS

Non-contact remote-sensing radiation thermometry was used in the applications of temperature measurement in ceramics grinding and diesel exhaust aftertreatment filters. Different radiometric methods, including spectrometer (multi-wavelength), one color (single wavelength) and two color (two wavelength) methods, were developed for measuring surface temperatures in the two industrial applications. The spectrometer method was employed to measure the grit-workpiece interface temperatures in MgO-PSZ grinding. Both one-color and two-color methods were developed for measuring temperature distribution in diesel exhaust aftertreatment filters.

The spectrometer method was developed to measure the grit-workpiece interface temperatures for grinding 9 mol % MgO-PSZ. Advantage was taken of the fact that PSZ is semi-transparent in the near infrared and measurements were made using transmitted light. Effective temperatures on the order of 3000 K were obtained for the grinding conditions used. Simulations were made which showed that the effective temperatures measured are representative of the peak hot-spot temperatures reached during grinding. This is consistent with high grinding chip temperatures, which result from the very low thermal conductivity of PSZ. The high chip temperature causes reversion of the monoclinic phase to tetragonal phase in the grinding chips, whereas the ground surfaces contain excess monoclinic phase. Very high chip temperatures can also produce ductile-like grinding response. This effect appears to underlie the success for SiC-grinding of PSZ components in high-volume production applications.

A fiber optic radiation thermometry system was developed to measure the channel wall surface temperature in a diesel exhaust aftertreatment filter. Based on two wide-band infrared PbS and PbSe detectors, the system is able to measure temperatures ranging from 100 to 400°C in the filter channel with large aspect ratios. If a lock-in amplifier is used, the low temperature measurement capability of the system can be further improved. Experimental results show the sensor's lower temperature measurement limit is as low as 70°C to 80°C with a lock-in amplifier added. By employing a sapphire fiber with 45° angled tip, the thermal radiation from a small and specific region opposite the polished tip face and perpendicular to the fiber axis can be measured. Both one-color and two-color thermometry methods were implemented in this study. The two-color method generally predicted higher temperature than the one-color method. The discrepancy between the two temperature measurement methods was small for the channel with large aspect ratio or near blackbody characteristics. Experimental results show that the system is suitable for the non-contact, in-situ temperature measurement for diesel exhaust aftertreatment filters.

Based on the above temperature measurement results, the infrared thermometry method was applied to study of temperature distribution in microwave assisted diesel particulate filter regeneration. Temperature measurement tests were performed by the integration of a multi channel fiber optic infrared temperature measurement system and a microwave heating system. Instead of thermocouples, Silica light-pipes, which are transparent to the microwave electromagnetic field, are used to collect infrared radiation inside filter cavities.

Three advanced DPFs were heated with microwaves and, the measured temperature profiles were studied. Experimental results show non-uniform heating across the filter. The

temperature distribution in these filters was similar to modeling results. The interaction between catalyst, soot loading, and microwave power changes the heating pattern and temperature level. During a 600 s heating period, a 1 kW microwave power setting was able to raise the temperatures above 200°C in most area of a catalyzed filter with soot loading. The temperature profiles obtained in this study have provided important data for filter materials and cavity development to further reduce temperature gradients during microwave assisted DPF regeneration.

The temperature measurement results of diesel exhaust aftertreatment filters Lead to a better understanding of diesel exhaust aftertreatment regeneration mechanism and process and, provide the data for study of NO<sub>x</sub> and particulate filter reliability and durability, thermal cycle fatigue, and modeling of the regenerative temperature distribution. On-going research of the development is to implement this system in an operating diesel exhaust aftertreatment filter with exhaust flow, soot deposition, and coated catalysts. The filter will be subject to hot exhaust gas and experience temperature cycling while capturing and regenerating the NO<sub>x</sub> or particulates.

## Appendix

When the approximation shown in Eq. (2.4) is invalid, the linear regression method corresponding to Eq. (2.5) cannot be used. In order to deal with this case, consider the general form for the least-squares deviation,  $\Delta$ , given by

$$\Delta(T, S) = \int (SR - E)^2 d\lambda \quad (\text{A1})$$

The integral is to be evaluated over the spectrometer wavelength measurement range.  $R(\lambda)$  is the measured spectrometer function,  $S$  is the scaling factor and  $E(\lambda, T)$  is the blackbody function in Eq.(2.3). Minimization to obtain the best fit of the scaled spectrometer function to the blackbody curve must be done over a 2-D parameter space for  $S$  and  $T$ , hence,

$$\left( \frac{\partial \Delta}{\partial S} \right)_T = 0 \quad (\text{A2})$$

$$\left( \frac{\partial \Delta}{\partial T} \right)_S = 0 \quad (\text{A3})$$

An explicit solution for  $T$  cannot be obtained, however, using Eq. (A1), Eq. (A2) can be solved explicitly for  $S$ .

$$S = \frac{\int ERd\lambda}{\int R^2 d\lambda} \quad (\text{A4})$$



Equation (A4) is the best-fit value of S for any given value of T, therefore, we can reduce the problem to 1-D minimization for T. Substituting Eq. (A4) into Eq. (A1) gives

$$\Delta(T) = \int E^2 d\lambda - \frac{\left[ \int ER d\lambda \right]}{\int R^2 d\lambda} \quad (\text{A5})$$

Equation (A5) can be evaluated numerically for specified values of T. The required value of T is obtained for the minimum deviation. As an illustration, the spectrometer data shown in Fig. 2.4(c) were analyzed using Eq. (A5). For convenience, the spectrometer function  $R(\lambda)$  was represented by a second-order polynomial shown as the dashed line in Fig. 2.4(c). After substituting the polynomial approximation for  $R(\lambda)$  into Eq. (A5), the integrals were evaluated numerically using standard mathematical integration routines (Maple V). The results are shown in Fig. A1. The value of T obtained at the minimum point (arrow) is 2909K. This can be compared to the value, 2923 K, obtained for the same data using the linear regression fit, Eq. (2.5). This small discrepancy is attributed to numerical differences arising between the two computational methods. Values of S and T obtained with deviations above or below the minimum at 2909 K correspond to the best-fit black body curves for these temperatures. These are shown in Fig. 2.6.

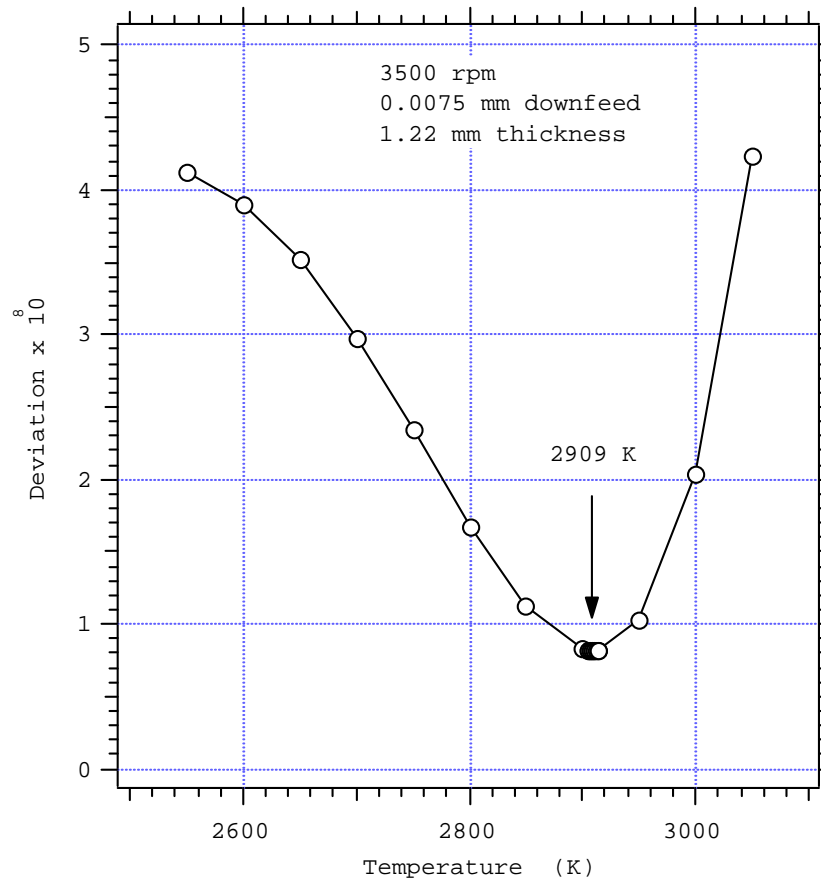


**Figure A1. Simulation results for deviation vs. temperature**